Validating 70 Million Years of Convection Driven True Polar Wander and Dynamic Flattening with Paleomagnetic Data

Alessandro Forte

University of Florida, Institut de Physique du Globe de Paris https://orcid.org/0000-0002-3530-0455

Petar Glišović

Institut de Physique du Globe de Paris

Marianne Greff-Lefftz

Institut de Physique du Globe de Paris

Shayan Kamali Lima

Université Paris Cité, Institut de Physique du Globe de Paris

David Rowley

Univeristy of Chicago https://orcid.org/0000-0001-9767-9029

Physical Sciences - Article

Keywords:

Posted Date: January 13th, 2025

DOI: https://doi.org/10.21203/rs.3.rs-5397333/v1

Additional Declarations: There is **NO** Competing Interest.

Title:

Validating 70 Million Years of Convection Driven True Polar Wander and Dynamic Flattening with Paleomagnetic Data

Authors:

Alessandro Forte*[1,2,3], Petar Glišović [2,3,4], David Rowley[†, 5], Marianne Greff[2], Shayan Kamali Lima[2]

* Corresponding author, email: forte@ufl.edu, forte@ipgp.fr

[1] Department of Geological Sciences, University of Florida, Gainesville, FL, 32611, USA [2]

Université Paris Cité, Institut de Physique du Globe de Paris, 75238 Paris Cedex 05, France

[3] GEOTOP, Université du Québec à Montréal, Montréal, QC, H3C 3P8, Canada.

[4] Dept. of Geological Sciences & Geological Engineering, Queen's University, Kingston, ON, K7L 3N6, Canada

[5] Department of the Geophysical Sciences, The University of Chicago, Chicago, IL, 60637, USA

[†] David Rowley, deceased May 30, 2024

Abstract:

Mantle convection drives changes in Earth's ellipsoidal figure and corresponding moment of inertia, causing shifts in the planet's rotation axis known as true polar wander (TPW). Using seismic tomography and the Back-andForth Nudging (BFN) method, we developed a time-dependent convection model that reconstructs the evolution of mantle density distribution and Earth's moment of inertia over the past 70 million years. This modelling approach provides a close match with independent paleomagnetic constraints on the Cenozoic shifts of Earth's rotation pole, specifically resolving the previously unexplained U-turn in TPW trajectory at approximately 50 million years ago. Our findings reveal TPW shifts exceeding 5 degrees, despite the temporal stability imposed by high lower-mantle viscosity and the stabilizing effect of Earth's remnant rotational bulge. Verification of our predicted changes in Earth's ellipsoidal figure through independent paleomagnetic data provides a robust calibration for new predictions of convection-induced dynamic flattening variations. Over the past 70 million years, we find convection-induced

changes of flattening that shift from -0.2% to +0.1 % during the Paleogene. Our predictions of precession frequency in the Paleogene align with recent independent cyclostratigraphic studies, thus validating our model's accuracy and supporting the hypothesis of reduced tidal dissipation during this period.

Introduction

Mantle convection governs the movement of heat and mass within Earth's ~2890 km-thick mantle, influencing fundamental geophysical processes such as the planet's gravity field and rotational dynamics. Through its impact on Earth's moment of inertia, mantle convection induces shifts in the planet's rotation axis, known as 'true polar wander' (TPW), and induces changes in its elliptical figure, quantified as a 'dynamic flattening', that influences the slow conical precession of Earth's rotation axis.

The relationship between Earth's rotation and its internal structure has been a longstanding focus of geophysical research. In *Milankovitch's (1934)* exploration of the rotational influence of continental and oceanic masses alone, he demonstrated how the rotation axis may align with the direction of the maximum moment of inertia dictated by these masses, resulting in polar motion that traces a predictable path over time. The seminal work of *Munk and MacDonald (1960)* first highlighted the potential for deep-seated dynamics, in particular mantle convection, to influence Earth's rotational stability, including TPW. This link between mantle convection and TPW was explored in greater detail by *Goldreich & Toomre (1969)*, who further advanced the understanding of how any slow, internally driven changes to Earth's ellipsoidal shape will cause significant angular displacements of the planet's rotation axis as it seeks to remain aligned with the principal axis of inertia with the largest moment. They demonstrated that convection-induced changes in Earth's moment of inertia drive secular motion of the poles with the rotational bulge acting as a stabilizing force.

Mantle Dynamics and TPW Stabilization

Subsequent studies have shown that subducting lithospheric masses and very deep structures like Large Low Shear Velocity Provinces (LLSVPs) create significant mass imbalances that influence Earth's inertia tensor and therefore TPW. *Spada et al. (1992)* and *Ricard et al. (1993)* quantitatively linked subducted slabs to the excitation of TPW, demonstrating that mass anomalies generated by subduction can produce observable shifts in Earth's rotation axis.

These studies also highlighted the stabilizing role of the rotational bulge, which modulates the magnitude of TPW. *Richards et al. (1997)* demonstrated, however, that the long-term stability of Earth's rotational axis is primarily governed by the slow reorganization of subducted slabs rather than adjustments of the rotational bulge. In a parallel study that modelled the advection of mantle density heterogeneities inferred from seismic tomography, it was again found that the rate of polar motion is controlled by mantle viscosity and density distribution changes (*Steinberger & O'Connell, 1997*). Later research by *Steinberger and Torsvik (2010)* and *Greff-Lefftz and Besse (2014)*, expanded on this by linking mantle dynamics, particularly the interaction between LLSVPs and subduction, to long-term polar wander behavior. *Rouby et al. (2010)* also highlighted the key role that the evolution of subducted slabs and LLSVPs plays in shaping Earth's geoid and inertia axes. Their work emphasized the importance of these mantle structures in controlling the observed TPW behavior, although they noted discrepancies when compared to paleomagnetic data, pointing to the need for further progress in modelling convection-driven density contrasts in the mantle.

Matsuyama et al. (2006) demonstrated that the presence of an elastic lithosphere introduces significant resistance to reorientation of the planetary rotation axis and hence limits TPW. Extending this work, *Chan et al. (2011)* demonstrate the stabilizing effects that may arise from a remnant rotational bulge and excess ellipticity, which can limit the amount of TPW on Earth. Additionally, *Creveling et al. (2012)* showed that interaction between convectively driven inertia perturbations and elastic lithosphere stabilization could result in complex oscillatory paths, potentially explaining some abrupt shifts in Earth's rotational behavior during key geological periods. *Rose and Buffett (2017)* highlighted how TPW rates are controlled by mantle viscosity and the rate of mass redistribution within the mantle.

Paleomagnetic Constraints and Challenges

In addition to the theoretical and numerical models discussed above, paleomagnetic studies provide critical observational constraints on TPW and hence on the evolution of Earth's ellipsoidal figure. Comprehensive analyses, such as those by *Besse and Courtillot (2002)* and *Torsvik et al. (2012)*, offer independent observational records of Earth's past rotational axis shifts. These data serve as fundamental benchmarks for validating the predictions of mantle convection models. The ability of a model to reproduce the observed TPW, including key

features like a U-turn in the pole trajectory around 50 Ma, is a crucial test of its accuracy and robustness. Reconciling these paleomagnetic observations with mantle convection models remains an outstanding challenge due to uncertainties in the paleomagnetic data and the theoretical and numerical difficulties encountered in developing sufficiently realistic simulations of the time-dependent evolution of mantle convection.

While earlier geodynamic models provided insights into how mantle processes drive polar wander, they often struggled to capture specific features of Earth's TPW history. Models such as those developed by *Cambiotti et al. (2011)* emphasized the importance of considering the delayed response of Earth's rotational bulge and viscoelastic properties when modeling TPW, leading to more realistic predictions of Earth's rotational behavior. Similarly, *Steinberger et al. (2017)* provided valuable insights into the interaction between mantle convection and the stabilizing role of Earth's triaxial shape, but their model predictions of TPW over the past 70 million years significantly overestimated the observed paleomagnetic data, highlighting the need for more accurate reconstructions of mantle dynamics – a gap our study seeks to address. Significant discrepancies between predicted and observed TPW therefore persist, in particular the enigmatic U-turn in TPW around 50 million years ago remains unexplained.

A New Approach

In this study, we build upon the foundational works reviewed above by employing a time-dependent thermal convection model that utilizes the Back-and-Forth Nudging (BFN) method (*Glisovic & Forte 2016*). This approach, which incorporates seismic tomography models as an initial condition, allows us to reconstruct the 4-D evolution of Earth's mantle structure and moment of inertia over the past 70 million years with an accuracy that has been verified against present-day geodynamic observables and major geologic events during the Cenozoic. Our mantle convection reconstructions underwent successful ground truthing of both their temporal and spatial realism, notably in previous studies that investigated the origins and evolution of the Deccan Traps (*Glisovic & Forte 2017*), the North Atlantic Igneous Province (*Glisovic & Forte 2019*), the Nile River drainage basin (*Faccenna et al. 2019*) and, most recently, the origin and growth of the Antarctica geoid-low during the Cenozoic Era (*Glisovic & Forte 2024*).

The BFN modelling allows us, in the work presented below, to reconstruct the 70-million-year evolution of Earth's ellipsoidal figure and moment of inertia, and hence predict new TPW trajectories over this time interval that achieve a good match between model predictions and independent paleomagnetic data. Most importantly, as we document in the following, our model successfully captures the U-turn in TPW around 50 Ma, a phenomenon that has eluded previous models.

Convection-Induced Dynamic Flattening

Our reconstructions of the evolution of Earth's ellipsoidal figure using the BFN models directly yield predictions for the evolution of Earth's dynamic flattening that controls the astronomical precession of Earth's rotation axis (see the *Supplementary Information*, henceforth '*SI*'). These dynamic flattening changes will be directly calibrated through matching of the predicted TPW trajectories against the independent paleomagnetic constraints on Earth's pole positions. Dynamic flattening affects Earth's precession of the equinoxes by determining how lunisolar gravitational torques act on the planet's equatorial bulge, driving a slow wobble of Earth's rotation axis. This precession, along with changes in obliquity (Earth's axial tilt), modulates the latitudinal distribution of solar radiation, and thus plays a crucial role in the Milankovitch paleoclimate cycles (*Pälike & Shackleton 2000*, *Hinnov 2013, Farhat et al. 2022a*). Early models, such as those by *Forte & Mitrovica (1997)*, proposed that mantle convection could significantly influence Earth's moment of inertia and hence dynamical flattening, potentially inducing orbital resonances with Jupiter and Saturn, previously theorized by *Laskar et al. (1993)*, that contribute to long-term climate variability.

Morrow et al. (*2012*) later investigated the combined influences of glacial isostatic adjustment (GIA) and mantle convection over the past 25 million years. Their findings indicated more moderate, time-averaged variations in dynamic flattening, which proved difficult to reconcile with independent cyclostratigraphic data. This discrepancy introduced a challenging "enigma" regarding the relationship between observational evidence of dynamic flattening's evolution and the underlying geodynamic processes responsible for these changes.

More recently, *Ghelichkhan et al. (2021)* utilized a 4-D variational reconstruction of the past evolution of mantle convection to model Earth's precession constant over the last 50 million years, again suggesting modest convection-induced changes (~0.2%) to the dynamic flattening. This study did not extend to the beginning of the

133 Cenozoic, in particular the period preceding and including the Paleocene-Eocene Thermal Maximum at 56 Ma,
134 and it was not calibrated against independent paleomagnetic constraints on moment of inertia changes, leaving
135 open questions about Earth's long-term rotational evolution during this key time interval (*Boulila & Hinnov 2022*).
136
137 **BFN Modelling Results**
138 To model the dynamic origin and temporal evolution of Earth's ellipsoidal gravitational figure and related moments
139 of inertia, we reconstructed the 4-D evolution of mantle convection throughout the Cenozoic era using an iterative
140 BFN method for time-reversed, tomography-based convection (*Glisovic & Forte 2016*). This time-reversed mantle
141 convection methodology is summarised in the *Methods* section. We nonetheless underline here an important
142 technical point that is worth keeping in mind. The BFN methodology yields a global reconstruction of the mantle's
143 3-D structure at some desired time in the past: here 70 million years ago. This reconstructed past state is then used
144 as the starting point for a mantle convection calculation that advances forward in time, from the past to the present.
145 It is from this complete forward simulation, that fully satisfies the equation of thermal energy conservation in the
146 mantle, that we reconstruct the changing ellipsoidal figure and related moments of inertia, that are analyzed in the
147 following discussion.
148 Paleomagnetic reconstructions of Earth's rotation axis over the past 200 million years, based on the geocentric
149 axial dipole model, have provided valuable constraints on True Polar Wander (TPW). However, these
150 reconstructions are subject to significant uncertainties, particularly when determining the precise trajectory of the
151 rotation axis (see *Methods* and Table 1). Despite these uncertainties, we aim to assess whether paleomagnetic
152 constraints on Earth's rotation align with the changes predicted by mantle convection models during the Cenozoic
153 Era.
154 In Figure 1a, we present TPW trajectories predicted by reconstructions of mantle convection over the past 70
155 million years that use two mantle viscosity profiles (V1 and V2, shown in Fig. S1) and two global tomography
156 models (GyPSuM and S40RTS – see Methods). A key outcome is the distinct U-turn in Earth's rotation axis
157 trajectory that is observed at approximately 50 million years ago, which is captured in both the paleomagnetic data
158 (*Torsvik et al. 2012*) and our mantle convection models. The accuracy with which this U-turn is reproduced by the
159 convection reconstruction employing the V1 model, and initialized with the GyPSuM tomography model,

represents a significant advancement over previous convection models that were based on the history of subducted slabs and were unable to capture this key feature (*Rouby et al. 2010, Steinberger et al. 2017*). Additionally, we find that the sharp U-turn at 50 Ma is also predicted in the absence of a remnant rotational bulge and therefore is not dependent on the stabilization arising from long-term elasticity of the lithosphere (see Figure S2 in the *SI*).

In a further analysis of the TPW paths (see Figure 1b), we specifically focussed on the angular displacement of Earth's rotation pole relative to the present-day North Pole as a function of time. The V1 model closely tracks the paleomagnetic data, particularly around 50 Ma, where the maximum pole deviation occurs. This excellent alignment between model predictions and paleomagnetic data is further confirmed by the analysis in Table 2, where we observe a goodness of fit (see eq. 4 in *Methods*), analogous to the reduced chi-square fit, whose value is close to one for the past 70 million years. Figure 2 presents the relative deviation between the predicted and observed pole positions, normalized by the paleomagnetic uncertainty bounds (α95). The hybrid approach (eq. 1 in *Methods*) used in the *n-V1** and *m-V2** models, where present-day moment of inertia is combined with model predictions, appears to be key to achieving a closer match to the paleomagnetic data. Notably, the relative deviations for these models remain consistently below ~1.5 for much of the Cenozoic, suggesting they effectively capture the main features of Earth's rotational dynamics, including the U-turn around 50 Ma. Compared to previously published studies (e.g., *Rouby et al. 2010*), our model provides a substantially improved match to paleomagnetic data, both in the direction and magnitude of TPW excursions. This quantification of the fit provides robust validation of the model's predictions, indicating that our 70-million-year mantle convection reconstruction reproduces Earth's moment of inertia changes over geological timescales with good accuracy.

Figure 3 highlights the evolution of true polar wander (TPW) velocities over the past 70 million years, comparing observed interval-averaged velocities from paleomagnetic data with the best-fitting predictions (Table 2) from the BFN models, specifically n-V1* and n-V1, obtained using the differential and direct calculation of perturbed moment of inertia changes, respectively (see equations 1 and 2 in *Methods*). The TPW velocities derived from the paleomagnetic data (Table 1), shown by the green curve in Fig. 3, showing a peak between 60 and 50 Ma. This peak corresponds to the abrupt change in the rotation pole's direction, as indicated by the U-turn in the TPW path shown in Figure 1. The maroon and orange curves, representing predictions from the n-V1 and n-V1* models, similarly show this peak in TPW velocity near 50 Ma. The instantaneous velocities, represented by the dashed

curves, are computed using eq. (23) in the *SI* and they incorporate the transient response to the relaxing rotational bulge. Since the TPW calculations are initiated using an equilibrium pole position at 70 Ma, where the initial instantaneous TPW velocity is zero, the predicted instantaneous TPW velocities near 50 Ma will be muted relative to the interval-averaged velocities. The predicted interval-averaged velocities are therefore more closely aligned with the corresponding interval-averaged TPW velocity from paleomagnetic data, both in terms of magnitude and timing. These results, in Fig. 1 to Fig. 3, demonstrate the ability of the BFN modelling to replicate key features of Earth's rotational dynamics, including the U-turn in TPW near 50 Ma, and underscore the sensitivity of TPW to convection-induced changes in Earth's moment of inertia, which are modulated by the viscosity of the mantle.

One other noteworthy result presented in Figure 3, concerns the present-day rates of TWP predicted by the BFN reconstructions of mantle evolution over the past 70 million years and the present-day rates estimated from paleomagnetic constraints on TPW. These present-day rates, lying between 0.2 and 0.4°/Ma, represent between 20 to 40% of the 20th century TPW rate of about 1°/Ma determined by geodetic observations (*McCarthy & Luzum 1996*). These new findings contrast with previous studies that concluded that mantle convection explains at least 66% of the present-day TPW velocity (*Adhikari et al. 2018*).

The temporal evolution of Earth's moment of inertia, will also be manifested in changes in Earth's dynamical flattening, quantified as $\Delta H(t)/H_0$ (see eq. 5 in *Methods* and eq. 30 in the *SI*). Our BFN reconstructions of mantle convection-induced changes to the moment of inertia predict significant variability in Earth's dynamic flattening over the past 70 million years (Figure 4(a)). The n-V1 (and n-V1*) and S40RTS-m-V2* model predictions show 0.2 to 0.3% increase in dynamic flattening between 70 Ma and 30 Ma. This variability is comparable to that reported by *Ghelichkhan et al. (2021)*, who limited their mantle convection reconstructions to the past 50 million years. Similarly to *Ghelichkhan et al. (2021)*, our predictions show a modest 0.2% decrease in dynamical flattening from its peak value at 30 Ma to the present day (PD).

From cyclostratigraphic analyses of Eocene deep-sea sediment cores, *Boulila & Hinnov* (*2022*) inferred reductions in dynamical flattening that are compatible with reduced flattening predicted by mantle convection reconstructions (*Ghelichkhan et al. 2021*). Such inferences are, however, highly dependent on a robust quantification of much larger amplitude changes to flattening due to tidal-induced deceleration of Earth's rotation (see equation 48 and Figure S4(c) in *SI*) and are also dependent on potentially important complications (e.g. hiatus

events) affecting cyclostratigraphic interpretations (*De Vleeschouwer et al. 2023*). It is thus important to combine both mantle convection and tidal contributions to flattening, while recognizing that the latter may have strongly varied over the past 70 Ma due to major changes in ocean tidal dissipation (TD), as suggested by numerical models that incorporate geological estimates of Earth's paleogeographic evolution (*Green et al. 2017*).

The combined convection and tidally driven changes to dynamic flattening, quantified as $\Delta H(t)/H_0$ (see eq. 30 in the *SI*), are presented in Figure 4(b), where it is clear that TD is the dominant contribution to dynamic flattening changes over the past 70 Ma. Mantle convection generates a relatively modest modulation of the larger amplitude dynamic flattening variation due to TD. This conclusion is verified in three different scenarios that we explored: (1) present-day (PD) TD is assumed constant over the past 70 Ma (solid lines in Fig. 4(b)), (2) TD is reduced to 50% of PD for times earlier than 5 Ma (dashed lines in Fig. 4(b)), and (3) TD is reduced to 30% of PD for times earlier than 35 Ma (dash-dotted lines in Fig. 4(b)). Scenarios 2 & 3 (see discussion in section 9 of *SI*,) are motivated by the paleo-tidal numerical simulations by *Green et al.* (*2017*), who modelled the impacts of changing bathymetry and continental configurations during the Cenozoic (and earlier), including the opening of the Drake Passage and Tasman Gateway, and found TD was strongly reduced relative to PD. Scenario (1) is assumed in the *Laskar et al.* (*2004*) (henceforth 'La2004') many-body orbital solution. As shown in equation (6) in *Methods*, the axial precession frequency will vary directly with the ratio $H\ \Omega/\ \equiv \gamma$, therefore it is the timedependent change of this ratio relative to the PD value, $\Delta\gamma(t)/\gamma_0$, that is of greater relevance when the rotation rate changes significantly with time. In Figure 4(c) we therefore show the predicted variation of $\Delta\gamma(t)/\gamma_0$ for all three TD scenarios and we note the mantle-convection modulation of the tidally driven variations is enhanced relative to its contribution in Figure 4(b). We draw particular attention to scenario 3 (TD reduced to 30% of PD), where the flattening ratio $\Delta\gamma(t)/\gamma_0$ changes little from 70 to 40 Ma, because of the mantle convection modulation.

Finally, the implications of convection and TD for the predicted changes in Earth's axial precession frequency, ω_{prec} (see equation 6 in *Methods*), are shown in Figure 4(d), along with observational estimates of ω_{prec} in the Paleogene Period, inferred from cyclostratigraphic and astrochronological interpretations of Atlantic deep-sea sediment cores, including an outcrop from Spain ('Sopelana') with Cretaceous-Paleogene marine sediments (see figure caption for source references). While none of the three TD scenarios yield an optimal fit to the observational

240 estimates of ω_{prec}, we suggest that scenario 3 (TD reduced to 30% of PD, prior to 35 Ma) comes closest to
241 reconciling the data from the deep-sea cores and the 'Sopelana' outcrop. This inference is, of course, preliminary
242 and is based on a simplified parametrization of past changes in TD, here modelled with a piecewise-linear variation
243 and assuming only one transition time (i.e., 5 Ma or 35 Ma) in the past.
244
245 **Discussion & Conclusions**
246 Our study demonstrates a strong alignment between mantle convection models and paleomagnetic constraints on
247 true polar wander (TPW) over the Cenozoic Era, despite uncertainties in the paleomagnetic data and in the
248 geodynamic models. This agreement underscores the robustness of our time-dependent mantle convection
249 reconstructions and provides new insights into Earth's rotational dynamics. In particular, the marked U-turn in the
250 trajectory of Earth's rotation axis around 50 million years ago that points to a significant geodynamic
251 reorganization within Earth's interior during that period.
252 A critical strength of our study is that the same mantle convection reconstructions that predict the
253 timeevolution of Earth's moment of inertia tensor, used for true polar wander (TPW) predictions, are also used to
254 predict changes in dynamic flattening and associated precession frequency. Since both TPW and dynamic
255 flattening arise from the same moment of inertia tensor, which is perturbed by mantle convection, our ability to
256 accurately capture TPW dynamics verifies the reliability of our predictions of dynamic flattening changes.
257 Beyond validating our convection models, this work reveals modest but sustained changes in Earth's dynamic
258 flattening over the past 70 Ma. We predict a nearly 0.3% increase in convection-driven dynamic flattening between
259 70 Ma and 30 Ma, followed by a more gradual adjustment over the last 30 million years. The key question we then
260 addressed (in Figure 4(d)) is how these convection-induced changes in dynamic ellipticity, combined with past
261 variations in tidal dissipation, may influence the long-term evolution of Earth's precession frequency.
262 Cyclostratigraphic studies (*De Vleeschouwer et al. 2023*, *Wu et al. 2024*) provide critical data that help to
263 address this key question and provide support for the geodynamic model predictions. The reanalysis of Eocene
264 deep-sea sediment records (*De Vleeschouwer et al. 2023*) indicate that precession cycles – not obliquity cycles as
265 previously thought – dominate the lithological variations. This reinterpretation suggests lower tidal dissipation
266 rates during the Eocene, in agreement with our model predictions (and previous interpretations by *Boulila &*

Hinnov 2022) that also reveal enhanced mantle convection modulation when past TD is significantly lower (Figure 4(c) and (d)). These findings emphasize the importance of integrating both tidal and mantle dynamics to accurately model Earth's precessional changes. Discrepancies between cyclostratigraphic interpretations (*Boulila & Hinnov 2022, De Vleeschouwer et al. 2023*) underscore the complexity in deciphering sedimentary records.

We suggest that future progress would therefore benefit from the development of new astronomical solutions that integrate the predictions of precession-frequency changes derived from geodynamic models. Sedimentary records can then be re-analyzed using the modified astronomical models as tuning targets. Such refinements to the analysis of sedimentary frequencies would provide powerful tests of precession frequency variations predicted from the combined contributions of mantle convection and tidal dissipation. This integrated approach holds the potential to significantly advance both geodynamical modeling and the interpretation of sedimentary records, leading to a more comprehensive view of Earth's dynamical evolution.

Data Availability. All data analysed in this study were previously published in the cited references. Additional data related to this paper have been deposited at one of the University of Florida servers: link.

Code Availability. Viscous flow kernels required for nonhydrostatic geoid predictions have been deposited at one of the University of Florida servers: link.

Acknowledgments

We dedicate this paper in memory of David Rowley, friend and colleague who passed away during the preparation of this manuscript. His contributions to this work and his legacy and spirit continue to provide inspiration. The authors acknowledge the support provided by the French “Programme d’investissements d’avenir” under the auspices of the GYPTIS project – ANR 19 MPGA 0007 and the support provided by the Institut de Physique du Globe de Paris. AMF acknowledges support from the University of Florida and the support of this work provided by NSF grant EAR 1903108. PG acknowledges support from Queen’s University and the support of this work provided by the Stephen Cheeseman Geoselenic Research Project. PG and AMF also acknowledge the additional support provided by GEOTOP, Université du Québec à Montréal. The authors want to thank a number of

294 colleagues for extensive discussions related to mantle dynamics, surface geological evolution, and Earth's geoid:
295 Stephen Grand, Nathan Simmons, Shangxin Liu, and Alexander Braun. Their longstanding encouragement and
296 support of our work is gratefully acknowledged. The convection simulations in this study were carried out thanks
297 to supercomputing facilities of Digital Research Alliance of Canada and University of Florida.
298

References:

Adhikari, S., Caron, L., Steinberger, B., Reager, J. T., Kjeldsen, K. K., Marzeion, B., Larour, E. and Ivins, E.R. (2018). What drives 20th century polar motion? *Earth and Planetary Science Letters*, 502, 126-132.

Besse, J., & Courtillot, V. (2002). Apparent and True Polar Wander and the Geometry of the Geomagnetic Field Over the Last 200 Myr. *Journal of Geophysical Research: Solid Earth*, 107(B11), EPM-6.

Boulila, S., & Hinnov, L. A. (2022). Constraints on Earth-Moon dynamical parameters from Eocene cyclostratigraphy. *Global and Planetary Change*, 216, 103925.

Cambiotti, G., Ricard, Y., & Sabadini, R. (2011). New insights into mantle convection true polar wander and rotational bulge readjustment. *Earth and Planetary Science Letters*, 310(3-4), 538-543.

Chan, N. H., Mitrovica, J. X., Matsuyama, I., Latychev, K., Creveling, J. R., Stanley, S., & Morrow, E. (2011). The rotational stability of a convecting Earth: the Earth′ s figure and TPW over the last 100 Myr. *Geophysical Journal International*, 187(2), 773-782.

Creveling, J. R., Mitrovica, J. X., Chan, N. H., Latychev, K., & Matsuyama, I. (2012). Mechanisms for oscillatory true polar wander. *Nature*, 491(7423), 244-248.

De Vleeschouwer, D., Penman, D. E., D'haenens, S., Wu, F., Westerhold, T., Vahlenkamp, M., ... & Hull, P. M. (2023). North Atlantic drift sediments constrain Eocene tidal dissipation and the evolution of the Earth-Moon system. *Paleoceanography and Paleoclimatology*, 38(2), e2022PA004555.

Faccenna, C., Glišović, P., Forte, A., Becker, T. W., Garzanti, E., Sembroni, A., & Gvirtzman, Z. (2019). Role of dynamic topography in sustaining the Nile River over 30 million years. *Nature Geoscience*, 12(12), 10121017.

Farhat, M., Laskar, J., & Boué, G. (2022a). Constraining the Earth's dynamical ellipticity from ice age dynamics. *Journal of Geophysical Research: Solid Earth*, 127(5), e2021JB023323.

Forte, A. M., & Mitrovica, J. X. (1997). A resonance in the Earth's obliquity and precession over the past 20 Myr driven by mantle convection. *Nature*, 390(6661), 676-680.

Ghelichkhan, S., Fuentes, J. J., Hoggard, M. J., Richards, F. D., & Mitrovica, J. X. (2021). The precession constant and its long-term variation. *Icarus*, 358, 114172.

Glišović, P., & Forte, A. M. (2016). A new back-and-forth iterative method for time-reversed convection modeling: Implications for the Cenozoic evolution of 3-D structure and dynamics of the mantle. *Journal of Geophysical Research: Solid Earth*, 121(6), 4067-4084.

Glišović, P., & Forte, A. M. (2017). On the Deep-Mantle Origin of the Deccan Traps. *Science*, 355(6324), 613–616.

Glišović, P., & Forte, A. M. (2019). Two Deep-Mantle Sources for Paleocene Doming and Volcanism in the North Atlantic. *Proceedings of the National Academy of Sciences*, 116(27), 13227–13232.

Glišović, P., & Forte, A. M. (2024). The Cenozoic Evolution of Earth's Strongest Geoid Low: Insights into Mantle Dynamics below Antarctica, *Science Advances, in review*.

Goldreich, P., & Toomre, A. (1969). Some Remarks on Polar Wandering. *Journal of Geophysical Research*, 74(10), 2555–2567.

Green, J. A. M., Huber, M., Waltham, D., Buzan, J., & Wells, M. (2017). Explicitly modelled deep-time tidal dissipation and its implication for Lunar history. *Earth and Planetary Science Letters*, 461, 46-53.

Greff-Lefftz, M., & Besse, J. (2014). Sensitivity experiments on True Polar Wander. *Geochemistry, Geophysics, Geosystems*, 15(12), 4599-4616.

Hinnov, L. A. (2013). Cyclostratigraphy and its revolutionizing applications in the earth and planetary sciences. *GSA Bulletin*, 125(11-12), 1703-1734.

Laskar, J., Joutel, F., & Boudin, F. (1993). Orbital, precessional, and insolation quantities for the Earth from −20Myr to +10 Myr. *Astronomy and Astrophysics*, 270(1-2), 522-533.

Laskar, J., Robutel, P., Joutel, F., Gastineau, M., Correia, A. C., & Levrard, B. (2004). A long-term numerical solution for the insolation quantities of the Earth. *Astronomy & Astrophysics*, 428(1), 261-285.

Matsuyama, I., Mitrovica, J. X., Manga, M., Perron, J. T., & Richards, M. A. (2006). Rotational stability of dynamic planets with elastic lithospheres. *Journal of Geophysical Research: Planets*, 111(E2).

McCarthy, D. D., & Luzum, B. J. (1996). Path of the mean rotational pole from 1899 to 1994. *Geophysical Journal International*, 125(2), 623-629.

Milankovitch, M. (1934). Der Mechanismus der Polverlagerungen und die daraus sich ergebenden Polbahnkurven. In: *Handbuch der Geophysik*, Band 2, 1934, pp. 193–206.

Morrow, E., Mitrovica, J. X., Forte, A. M., Glišović, P., & Huybers, P. (2012). An enigma in estimates of the Earth's dynamic ellipticity. *Geophysical Journal International*, 191(3), 1129-1134.

Munk, W. H., & MacDonald, G. J. F. (1960). *The Rotation of the Earth: A Geophysical Discussion.* Cambridge University Press.

Pälike, H., & Shackleton, N. J. (2000). Constraints on astronomical parameters from the geological record for the last 25 Myr. *Earth and Planetary Science Letters*, 182(1), 1-14.

Ricard, Y., Spada, G., & Sabadini, R. (1993). Polar wandering of a dynamic Earth. *Geophysical Journal International*, 113(2), 284-298.

Richards, M. A., Ricard, Y., Lithgow-Bertelloni, C., Spada, G., & Sabadini, R. (1997). An explanation for Earth's long-term rotational stability. *Science*, 275(5298), 372-375.

Rose, I., & Buffett, B. (2017). Scaling rates of true polar wander in convecting planets and moons. *Physics of the Earth and Planetary Interiors*, 273, 1-10.

Rouby, H., Greff-Lefftz, M., & Besse, J. (2010). Mantle dynamics, geoid, inertia and TPW since 120 Myr. *Earth and Planetary Science Letters*, 292(3-4), 301-311.

Spada, G., Ricard, Y., & Sabadini, R. (1992). Excitation of true polar wander by subduction. *Nature*, 360(6403), 452-454.

Steinberger, B., & O'Connell, R. J. (1997). Changes of the Earth's rotation axis owing to advection of mantle density heterogeneities. *Nature*, 387(6629), 169-173.

Steinberger, B., & Torsvik, T. H. (2010). Toward an explanation for the present and past locations of the poles. *Geochemistry, Geophysics, Geosystems*, 11(6).

Steinberger, B., Seidel, M. L., & Torsvik, T. H. (2017). Limited true polar wander as evidence that Earth's nonhydrostatic shape is persistently triaxial. *Geophysical Research Letters,* 44(2), 827-834.

Torsvik, T. H., Van der Voo, R., Preeden, U., Mac Niocaill, C., Steinberger, B., Doubrovine, P. V., & Meert, J. G. (2012). Phanerozoic Polar Wander, Palaeogeography and Dynamics. *Earth-Science Reviews*, 114(3-4), 325–368.

Wu, Y., Malinverno, A., Meyers, S. R., & Hinnov, L. A. (2024). A 650-Myr history of Earth's axial precession frequency and the evolution of the Earth-Moon system derived from cyclostratigraphy. *Science Advances*, 10(42), eado2412.

Methods

To solve the direct (forward-in-time) problem of thermal convection in Earth's mantle, we use the governing equations that satisfy conservation of mass, momentum, and energy for a Newtonian viscous fluid in a compressible and self-gravitating mantle, employing a pseudo-spectral numerical method (*Glišović et al. 2012*). Detailed explanations of the pseudo-spectral solution of the regularized time-reversed energy equation are presented in *Glišović & Forte (2016)*.

All flow computations are carried out using spherical harmonic expansions up to a maximum harmonic degree of 170. This yields a horizontal spatial resolution varying from ~64 km at the core-mantle boundary (CMB) to ~117 km at the top of the mantle. The vertical resolution is defined using a Chebyshev polynomial expansion up to order 129, which provides a radial resolution from ~0.4 km near the isothermal boundaries to ~35 km in the mid-mantle.

The reference structure (density, gravity, thermal conductivity, heat capacity, and thermal expansion) follows *Glišović et al. (2012)*. Energy sources, including radioactive and secular cooling contributions, are uniformly distributed across all depths, providing a total energy budget of 24 TW.

As discussed in *Glišović & Forte (2014, 2016)*, the resolution of lateral variations in the upper mantle from seismic tomography, particularly their amplitudes, is often insufficient due to damping effects inherent in tomographic inversions. Thus, seismically inferred lateral temperature variations may not be in thermodynamic equilibrium with the steep radial temperature gradients in the thermal boundary layers (TBLs) within the lithospheric mantle and near the CMB. To mitigate the instability introduced by this lack of balance, we employed a purely adiabatic geotherm without (upper and bottom) TBLs, minimizing potential inaccuracies during backward modeling. The adiabatic geotherm was constructed based on temperature constraints at the upper mantle transition zone from *Katsura et al. (2004)*, where temperatures at the phase transitions at 410 km and 660 km depths are 1760 K and 1880 K, respectively. Surface and CMB conditions are isothermal, with a surface potential temperature of 1600 K and an adiabatic temperature of 2456 K at the CMB.

The depth-dependent viscosity models used in our calculations, shown in Fig. S1 in the *SI*, have been tested against a wide range of geodynamic constraints (*Mitrovica & Forte 2004; Forte et al. 2010*) and independent mineral-physical models (*Glišović et al. 2015*). In the calculations presented in this study, we specifically employ

the ‘V1’ viscosity profile, inferred by *Mitrovica & Forte* (*2004*) and the ‘V2’ viscosity profile (*Forte et al. 2010*). A discussion of both profiles and their geodynamic implications is presented in *Forte et al.* (*2015*).

The mechanical surface boundary condition assumes plate-like behavior, with viscous coupling between plate motions and the underlying mantle flow, ensuring that mantle flow drives the plates (*Forte & Peltier 1994, Forte et al. 2015*). The input for this coupling comes from the history of plate geometries throughout the Cenozoic, as derived from ocean floor ages and magnetic anomalies (*Rowley et al. 2016*). Plate reconstructions are based on the Indo-Atlantic hotspot reference frame, sampled at 5 Myr intervals, and all models are calculated in the no-netrotation (NNR) frame of reference. This boundary condition produces nearly equal amounts of poloidal (convergent/divergent) and toroidal (strike-slip) flows in the upper mantle (*Forte & Peltier 1994*).

Geologically reconstructed plate velocities provide the only direct constraints on the past evolution of 3D mantle buoyancy. Therefore, we developed an inverse procedure to determine the minimal perturbations required to match geologically inferred plate motions at selected instants (*Glišović & Forte 2016*). This method allows us to map regions in the mantle where small nudges to the buoyancy field can reproduce the geological plate motion data. This approach allows us to maintain mechanical and dynamical self-consistency by ensuring that all plate motions are, at any time, entirely driven by internal buoyancy forces.

The key input for mantle convection simulations is the 3D distribution of lateral density (and corresponding temperature) anomalies derived from the GyPSuM global tomography model, which integrates seismic, geodynamic, and mineral-physical data (*Simmons et al. 2010*). To quantify the uncertainties in our predictions, arising from imperfect resolution of mantle heterogeneity by seismic tomography, we also employ another tomography model, S40RTS (*Ritsema et al. 2011*). This model was derived exclusively from global seismic data that constrain the relative perturbations of seismic shear velocity in the mantle. Therefore, to evaluate the geodynamic implications of this model it is necessary to determine, *a-posteriori*, a scaling ratio that converts shearvelocity anomalies into equivalent density anomalies. In past studies, this scaling ratio is often assumed to have one value throughout the mantle, approximately estimated from mineral physics data. We instead ensure maximum geodynamic consistency of S40RTS by carrying out an Occam-style inversion of present-day geodynamic observables (gravity, topography, plate motions) to derive an optimal depth-dependent scaling ratio in the mantle.

The inversion procedure is described in *Forte et al.* (*2015*).

To reconstruct the temporal evolution of 3-D mantle heterogeneity, we use the quasi-reversibility (QRV) method, which integrates the governing conservation of energy equation backward in time. The QRV method, successfully applied in previous studies (*Glišović & Forte 2014, 2016, 2017*), reconstructs past temperature structures with errors below 10% for major observables like dynamic topography and gravity anomalies. To further refine our results, we couple the QRV method with the 'Back-and-Forth Nudging' (BFN) technique (*Glišović & Forte 2016*). This iterative method alternates between forward and backward integrations of the mantle convection model, spanning 2.5 Myr time windows, and iteratively updates the temperature field at each time step to minimize cumulative errors associated with thermal diffusion. The BFN method improves the resolution of mantle heterogeneity, allowing for more precise reconstructions of mantle dynamics over the past 70 million years.

The geodynamic consistency of our models is verified by comparing predictions of present-day surface signals (plate motions, gravity anomalies, and dynamic topography) against observations (*Glišović & Forte 2016*). Additionally, the 3D mantle structure is integrated forward from 70 Ma to the present day to confirm high global correlations with initial seismic-geodynamic models (*Glišović & Forte 2016*).

Ground truthing is a critical aspect of validating these model reconstructions. This includes verifying predictions against present-day geophysical observables such as the gravity/geoid anomalies and dynamic topography (*Glišović & Forte 2014, 2016*). We also establish temporal links between deep mantle upwellings and surface features, such as the Deccan Traps, the Nile River drainage basin, and the North Atlantic Igneous Province (*Faccenna et al. 2019; Glišović & Forte 2017, 2019*).

The ellipsoidal gravitational figure and related moments of inertia of the Earth are manifested in the longest wavelength geoid undulations corresponding to spherical harmonic degree 2 (see equation 5 in the SI). These geoid undulations are computed, at each instant in time, from our reconstructed distribution of internal mantle density anomalies employing mathematical kernel functions that represent the viscous-flow response of a compressible mantle that also account for all self-gravitational loads (*Forte et al. 2015*).

We calculated the convection-driven perturbations to Earth's time-dependent moment of inertia tensor, $\delta I_{ij}(t)$, using two approaches: the 'differential' approach and the 'direct' approach. In the differential approach, the difference between the predicted moment of inertia at any given time in the past relative to the predicted moment

of inertia at the present day is added to the observed, present-day perturbation of moment of inertia: $\delta I_{ij}(t) = \delta I_{ijobs}(0) + \Delta I_{ijcon}(t)$ where $\Delta I_{ijcon}(t) = \delta I_{ijcon}(t) - \delta I_{ijcon}(0)$, (1)

where $\delta I_{ij}{}^{obs}(0)$ is the present-day perturbation to the moment of inertia tensor determined from the degree-2 nonhydrostatic geoid derived from the GRACE geopotential solution (*Tapley et al. 2007*) and $\delta I_{ij}{}^{con}(t)$ is the inertia tensor perturbation predicted by the mantle convection model. The non-hydrostatic geoid is determined relative to Earth's hydrostatic ellipsoidal figure arising from the diurnal rotation (*Chambat et al., 2010*). The justification for the differential approach in equation (1) is that mantle convection alone does not entirely explain Earth's presentday moment of inertia because other geophysical sources, notably from crustal heterogeneity and glacial isostatic adjustment, also contribute. Moreover, there are inaccuracies in the reconstructed evolution of mantle structure that lead to an imperfect prediction for the present-day moment of inertia. The direct approach, on the other hand, calculates the perturbed moment of inertia entirely from the mantle convection reconstructions without any corrections, or allowance from other contributions (e.g., the crust):

$$\delta I_{ij}(t) = \delta I_{ij}{}^{con}(t)\,, \tag{2}$$

which may potentially lead to discrepancies in the predicted present-day pole position.

The numerical integration of the differential equation governing TPW driven by convection-induced perturbations to Earth's moment of inertia (see equation 23 in *SI*), requires the specification of input parameters related to the long-term viscous and elastic structure of the Earth. We calculate the time constant T_1 describing the long-term time dependence of the degree-2 tidal Love number (see equation 9 in *SI*), using the 'V1' and 'V2' radial viscosity profiles described above. For V1 we have $T_1 = 9.3$ kyr and for V2 we have $T_1 = 12.9$ kyr. These values are comparable to $T_1 = 11$ kyr calculated for a two-layer viscosity model, with upper-mantle viscosity equal to 10^{21} Pa-s and lower mantle that is 20 times more viscous (*Greff-Lefftz 2011*). The harmonic degree-2 tidal Love numbers in the fluid limit ($t \to \infty$), $k_f{}^T(LT)$, depend on the long-term elastic lithosphere thickness LT. We require two values in particular: $k_f{}^T(LT = 0) \equiv k^*{}_f{}^T$, the inviscid-fluid tidal Love number applicable to a purely hydrostatic planet, and $k_f{}^T(LT = 30\text{ km})$, where 30 km is a thickness compatible with the elastic-plate flexure modelling of

free-air gravity anomalies by *Watts & Moore (2017)*. This choice for the value of the elastic thickness, which exceeds the value $LT = 10$ km adopted in *Creveling et al. (2012)*, is discussed in the *SI* and the implications are illustrated in Figure S2. Numerical calculations of the degree-two tidal Love number in the fluid limit

(*Mitrovica et al. 2005*), employing the radial density profile in the PREM reference Earth model (*Dziewonski & Anderson 1981*), yield: $k^*{}_f{}^T = 0.9342$ and $k_f{}^T(LT = 30\ \text{km}) = 0.9319$. The 0.25% difference between these two values is what sustains a residual nonhydrostatic rotational flattening, termed the 'remnant bulge' by *Matsuyama et al. (2006)*, represented by equation (11) in the *SI*.

Our observational constraints on TPW are based on paleomagnetic data compiled and analyzed by *Torsvik et al. (2012)*. We estimate the TPW trajectory (in Table 1) over the past 80 Ma from the global apparent polar wander paths (GAPWP) determined from data in *Torsvik et al (2012)* and from the global rotations of *Rowley et al. (2016)*, and the *O'Neill et al. (2005)* rotations of plates relative to a fixed Indo-Atlantic hotspot frame. This TPW trajectory is calculated at 5-million-year time steps, with a 20-million-year moving window average of the paleomagnetic study mean data. We employ the statistical α_{95} values as an estimate of 95% confidence uncertainty, represented by the standard error of the mean of means. We recognize that these α_{95} likely underestimate the true uncertainties for several reasons. First, each study mean comprises some number of individual estimates of the mean with associated uncertainties. The study mean mean is the average of the individual estimates ignoring all of the uncertainties in the individual measurements. Second, the GAPWP mean at each time is the mean of the study means falling within the age interval window, again ignoring the uncertainties associated with each study mean. Third, there are uncertainties associated with each of the rotations of the plates needed to rotate data from each of the various major continents into a common frame of reference, including the rotation to the fixed hotspot reference frame. The correct summing of those uncertainties would yield a more realistic estimate of the true uncertainty. This uncertainty modelling should be the basis of a future study.

The extent to which the reconstructed temporal evolution of the convection-induced perturbations to Earth's moment of inertia are accurate and realistic, may be quantified by two measures of data fit. The first measure is the 'variance reduction' to the observed, present-day degee-2 nonhydrostatic geoid from the GRACE geopotential, defined as follows:

$$Var.Red.(\%) = 100 \times \left[1 - \frac{\sum_{m=2} \left\| (\delta N_o)_{m2p} - (\delta N_o)_{m2p} \right\|_2 (t=0) \right\|_2}{\sum_{m=2} \left\| (\delta N_o)_{m2p} \right\|_2 (t=0) \right\|_2}\right] \quad (3)$$

in which $(\delta N^o)_{m_2}$ and $(\delta N^p)_{m_2}(t=0)$ are, respectively, the degree-2 harmonic coefficients of the observed and predicted nonhydrostatic geoid at present day. A 100% variance reduction represents a perfect match between predicted and observed geoids. As discussed in the *SI*, notably equation (5), there is a direct linear relationship between the degree-2 geoid coefficients and Earth's moment of inertia tensor. The variance reduction defined in (3) thus quantifies whether the reconstructed 70-million-year evolution of mantle heterogeneity can successfully match the observed present-day nonhydrostatic geoid and hence the present-day moment of inertia.

Our second measure of fit, quantifies the 70-million-year match between the paleomagnetic determination of the TPW path and that predicted by the mantle convection reconstructions. This measure of 'goodness of fit' is analogous to the reduced chi-squared statistic and is defined as follows:

$$X^2_{TPW} = \frac{1}{N} \sum_{i=1}^{N} \left(\frac{\Delta\theta(t_i)}{\alpha 95(t_i)} \right)^2 \quad (4)$$

in which t_i $(i = 1 \ldots N)$ are the individual mean ages (see 2nd column in Table 1) for which a paleomagnetic pole position has been determined, $\Delta\theta(t_i)$ is the angular separation (in degrees) between the paleomagnetic pole position and the mantle convection prediction of the pole position at time t_i, and $\alpha 95(t_i)$ is the alpha-95 measure of uncertainty in the paleomagnetic pole position at time t_i. When $X^2_{TPW} \lesssim 1$, the mantle convection model is

526 fitting the paleomagnetic TPW trajectory within the data uncertainty. $X_{TPW}{}^2 >$ 1 indicates the fit by the predicted 527 TPW path has not fully captured the data or, alternatively, that the $\alpha 95$ underestimate the true uncertainties.

528 In the *SI*, we present the theoretical framework that we employed for modelling how mantle convection and 529 tidal dissipation influence Earth's rotational dynamics as manifested in Earth's time-dependent dynamic flattening 530 and precession frequency. Here, we briefly summarize the most important concepts and equations that underpin 531 our modeling results presented in Figure 4. The dynamic flattening, $H(t)$, represents the deviation of Earth's shape 532 from a perfect sphere due to centrifugal forces and internal dynamics. It is defined (see eq. 25 in *SI*) in terms of 533 Earth's principal moments of inertia $C(t) \geq B(t) \geq A(t)$ as follows:

534 $$H(t) = \frac{C(t) - \frac{1}{2}[A(t) + B(t)]}{C(t)} \quad (5)$$

535 This flattening parameter evolves over time due to changes in Earth's moment of inertia tensor produced by mantle 536 convection, which changes the mass distribution within the mantle, and from changes in centrifugal forces that

537 affect the entire planet, arising from the deceleration of Earth's rotation rate due to luni-solar tidal dissipation. 538 In all calculations presented in panels (b) – (d) in Figure 4, we employ the differential changes in Earth's 539 moment of inertia tensor expressed in equation (1) above. As underlined in the discussion following (1), the 540 present-day non-hydrostatic geoid contribution determined directly from the GRACE geopotential solution is held 541 fixed. This is also the case in our exploration of the impact of tidal deceleration on the moment of inertia tensor.

542 For the "purely tidal" modelling, the tidal changes to the inertia tensor (see equation 59 in *SI*) were calculated in 543 addition to the present-day non-hydrostatic contribution, $\delta I_{i,j}{}^{\mathrm{con}}(t = 0)$, that was held fixed over the entire 70 Ma

544 time interval we analyzed. This approach ensures that the present-day precession frequency (see equation 6, below) 545 agrees – in all simulations we performed – with the present-day reference value provided by the La2004 orbital 546 solution (see equation 72 in *SI*).

547 Earth's axial precession is the slow, conical movement of its rotational axis (similar to a wobbling spinning 548 top) caused by gravitational forces exerted by the Sun and Moon on Earth's equatorial bulge, where the latter is 549 quantified by the dynamical flattening in (5). The rate of this conical motion is quantified in terms of a precession 550 frequency, ω_{prec}, as follows (see also equation 71 and discussion in *SI*):

551 $$\omega_{prec} = \frac{3}{2}\frac{H}{\Omega}\left[\frac{GM_S}{\left(a_S\sqrt{1-e_S^2}\right)^3} + \frac{Gm_L}{\left(a_L\sqrt{1-e_L^2}\right)^3}\left(1-\frac{3}{2}\sin^2 i_L\right)\right]\cos\varepsilon \quad (6)$$

552 in which all parameters are defined in Table S1 in *SI*. This equation highlights how changes in dynamic flattening

553 H, Earth's rotation rate Ω , and the distance to the Moon a_L collectively affect the precession of Earth's rotation

554 axis. Earth's orbit is very stable on hundred-million-year time scales (*Zeebe 2015*) and therefore secular (i.e., non555 periodic) changes in the distance to Sun, a_S, are treated here as negligibly small.

556 The time evolution of the Earth-Moon distance, $a_L(t)$, is critical in understanding how tidal dissipation 557 impacts Earth's rotation rate and in modelling the precession frequency ω_{prec}, as shown in equation (6). We

558 modelled the evolution of $a_L(t)$ via the principle of conservation of vertical angular momentum in the Earth-Moon

559 system (see equation 67 and the related discussion in section 9 of the *SI*) as follows:

560 $$a_L(t) = \frac{\left[L_{total_{z,0}} - C_E(t)\,(\Omega_0 + \alpha_L\Omega_0 t)\cos\varepsilon\right]^2}{(m_L\cos i_L)^2\, GM_E\,(1-e_L^2)} \quad (7)$$

in which $L^{total}{}_{z,0}$ is the total vertical angular momentum of the Earth-Moon system, at present day, and is assumed to be constant, $C_E(t)$ is Earth's polar moment of inertia, Ω_0 is the present-day rotation rate, $\dot{\Omega}_0$ is the present-day deceleration rate, and $\alpha_L < 1$ is a (non-dimensional parameter) that represents the relative importance of lunar tidal dissipation relative to the combined total of lunar and solar tidal dissipation (see equation 63 in *SI*), and all other parameters are defined in Table S1. By combining mantle convection simulations with these equations that describe the effects of tidal forces, our theoretical approach (described in the *SI*) allows for a comprehensive analysis of Earth's rotational dynamics over the past 70 million years. This understanding is validated through comparison with independent observational data from paleomagnetism (Figures 1 – 3) and cyclostratigraphic studies (Figure 4(d)).

References (Methods):

Chambat, F., Ricard, Y., & Valette, B. (2010). Flattening of the Earth: further from hydrostaticity than previously estimated. *Geophysical Journal International*, 183(2), 727-732.

Dziewonski, A. M., & Anderson, D. L. (1981). Preliminary Reference Earth Model. *Physics of the Earth and Planetary Interiors*, 25(4), 297–356.

Forte, A. M., & Peltier, W. R. (1994). The kinematics and dynamics of poloidal-toroidal coupling in mantle flow: The importance of surface plates and lateral viscosity variations. *Advances in Geophysics*, 36, 1-119.

Forte, A. M., Quéré, S., Moucha, R., Simmons, N. A., Grand, S. P., Mitrovica, J. X., & Rowley, D. B. (2010). Joint Seismic-Geodynamic-Mineral Physical Modelling of African Geodynamics: A Reconciliation of DeepMantle Convection with Surface Geophysical Constraints. *Earth and Planetary Science Letters*, 295(3-4), 329–341.

Forte, A.M, Simmons, N.A, Grand, S.P. (2015) "Constraints on 3-D seismic models from global geodynamic observables: Implications for the global mantle convective flow," *Treatise of Geophysics*, G. Schubert, 2nd Ed. (Elsevier), vol. 1, pp. 853–907.

Glišović, P., Forte, A. M., & Moucha, R. (2012). Time-dependent convection models of mantle thermal structure constrained by seismic tomography and geodynamics: implications for mantle plume dynamics and CMB heat flux. *Geophysical Journal International*, 190(2), 785-815.

587 Glišović, P., & Forte, A. M. (2014). Reconstructing the Cenozoic evolution of the mantle: Implications for mantle
588 plume dynamics under the Pacific and Indian plates. *Earth and Planetary Science Letters*, 390, 146-156.
589 Glišović, P., Forte, A. M., & Ammann, M. W. (2015). Variations in grain size and viscosity based on vacancy
590 diffusion in minerals, seismic tomography, and geodynamically inferred mantle rheology. *Geophysical*
591 *Research Letters*, 42(15), 6278-6286.
592 Greff-Lefftz, M. (2011). Length of day variations due to mantle dynamics at geological timescale. *Geophysical*
593 *Journal International*, 187(2), 595-612.
594 Katsura, T., Yamada, H., Nishikawa, O., Song, M., Kubo, A., Shinmei, T., ... & Funakoshi, K. I.(2004). Olivine
595 wadsleyite transition in the system $(Mg,Fe)_2SiO_4$. *Journal of Geophysical Research: Solid Earth*, 109(B2).
596 Mitrovica, J. X., & Forte, A. M. (2004). A New Inference of Mantle Viscosity Based Upon Joint Inversion of
597 Convection and Glacial Isostatic Adjustment Data. *Earth and Planetary Science Letters*, 225(1-2), 177–189.
598 Mitrovica, J. X., Wahr, J., Matsuyama, I., & Paulson, A. (2005). The rotational stability of an ice-age earth.
599 *Geophysical Journal International*, 161(2), 491-506.
600 O'Neill, C., Müller, D., & Steinberger, B. (2005). On the uncertainties in hot spot reconstructions and the
601 significance of moving hot spot reference frames. *Geochemistry, Geophysics, Geosystems*, 6(4).
602 Ritsema, J., Deuss, A., van Heijst, H. J., & Woodhouse, J. H. (2011). S40RTS: A Degree-40 Shear-Velocity Model
603 for the Mantle from New Rayleigh Wave Dispersion, Teleseismic Traveltimes, and Normal-Mode Splitting
604 Function Measurements. *Geophysical Journal International*, 184(3), 1223–1236.
605 Rowley, D. B., Forte, A. M., Rowan, C. J., Glisovic, P., Moucha, R., & Grand, S. P. (2016). Kinematics and
606 Dynamics of the East Pacific Rise Linked to a Stable, Deep-Mantle Upwelling. *Science Advances*, 2(9),
607 e1601107.
608 Simmons, N. A., Forte, A. M., & Boschi, L. (2010). GyPSuM: A Joint Tomographic Model of Mantle Density and
609 Seismic Wave Speeds. *Journal of Geophysical Research: Solid Earth*, 115(B12), B12310.
610 Tapley, B. D., Bettadpur, S., Watkins, M., & Reigber, C. (2007). The Gravity Recovery and Climate Experiment:
611 Mission Overview and Early Results. *Geophysical Research Letters*, 31(9), L09607.
612 Watts, A. B., & Moore, J. D. P. (2017). Flexural isostasy: Constraints from gravity and topography power spectra.
613 *Journal of Geophysical Research: Solid Earth*, 122(10), 8417-8430.

615 Zeebe, R. E. (2015). Highly stable evolution of Earth's future orbit despite chaotic behavior of the Solar System.

616 *The Astrophysical Journal*, 811(1), 9.

Table 1: True Polar Wander Path for the Past 80 Myr Calculated With a 20-Myr Sliding Window Every 5 Myr†

Window (Ma)	*Age* (Ma)	*N*	*K*	α_{95}	K_{95}	θ (° N)	φ (° E)
10	6.9	49	126.62	1.82	12.44	87.05	164.32
15	13.1	33	102.53	2.48	13.83	85.79	158.09
20	18.3	28	89.93	2.89	14.76	85.64	152.99
25	25.5	22	113.75	2.92	13.13	85.99	154.18
30	29.6	23	134.38	2.62	12.08	85.43	151.24
35	34.9	23	103.66	2.99	13.75	84.63	151.9
40	39.6	22	101.77	3.09	13.88	84.52	158
45	45.6	24	87.71	3.18	14.95	83.54	133.65
50	51.8	32	77.13	2.91	15.94	82.38	140.5
55	56.7	41	87.89	2.39	14.93	84.31	158.31
60	59.8	46	76.65	2.42	15.99	84.97	191.55
65	63	44	101.94	2.14	13.87	84.39	195.76
70	65.8	33	105.13	2.45	13.65	85.59	208.95
75	71.6	22	118.31	2.86	12.87	86.14	234.8
80	81.8	25	83.02	3.2	15.37	86.72	239.06

† Calculated from GAPWP, based on data in *Torsvik et al. (2012),* using global rotations from *Rowley et al. (2016)* and *O'Neill et al. (2005)* rotations of plates relative to a fixed Indo-Atlantic hotspot reference frame.
Window: age (in Ma) of the centre of the window; *Age*: mean age computed from the data; *N*: number of studies; *K*: Fisher's precision parameter; α_{95}: uncertainty (in °) at the 95% confidence level; K_{95}: 95% confidence interval (in °) within which 95% of study means contributing to the GAPWP are expected to fall; θ, φ latitude and longitude of the pole positions

Table 2: Fits to 70-Million-Year Paleomagnetic TPW Path† and Present-Day Degree-2 Nonhydrostatic Geoid‡

Model / **Data**	GyPSuM n-V1*	GyPSuM m-V1*	GyPSuM m-V2*	GyPSuM m-V2*	S40RTS n-V1
Var. Red. ($l = 2$)	90%	90%	90%	80%	77%
X_{TPW}^2	1.4	0.95	1.3	3.8 (0.94 over 50Ma)	1.5

† TPW data consist of paleomagnetic determination of pole position, for each mean age, identified in Table 1.
‡ The $l = 2$ nonhydrostatic geoid coefficients are derived from the GRACE geopotential solution (*Tapley et al. 2007*), relative to the hydrostatic ellipsoid (*Chambat et al., 2010*).
* Denotes predicted TPW paths, shown in Fig. 1, that are based on calculations of the differential inertia tensor perturbations, as defined in equation (1) in *Methods*. Otherwise, the direct approach is used, defined by equation (2) in *Methods*. In this study, we employed two global tomography models as initial conditions for the mantle convection reconstructions: GyPSuM (*Simmons et al. 2010*) and S40RTS (*Ritsema et al. 2011*). Likewise, we also employed two geodynamic inferences of the depth-dependent mantle viscosity, V1 and V2, shown in Fig. S1 in the *SI*. The models denoted "m-", represent convection reconstructions in which mantle flow is constrained to match geological reconstructions of past plate motions (*Rowley et al. 2016*). The models denoted by "n" do not impose any matching to geologic inferences of past plate motions. In all cases, however, the models incorporate tectonic plates as a mechanical surface boundary condition, in which all plate motions are viscously coupled to mantle flow and driven by internal buoyancy.
Var. Red. is a measure of data fit, to the observed present-day degree-2 geoid, defined in equation (3) in *Methods*. Likewise, X_{TPW}^2 is a measure of fit to the paleomagnetic determination of the TPW path (Table 1), defined in equation (4) in *Methods*.

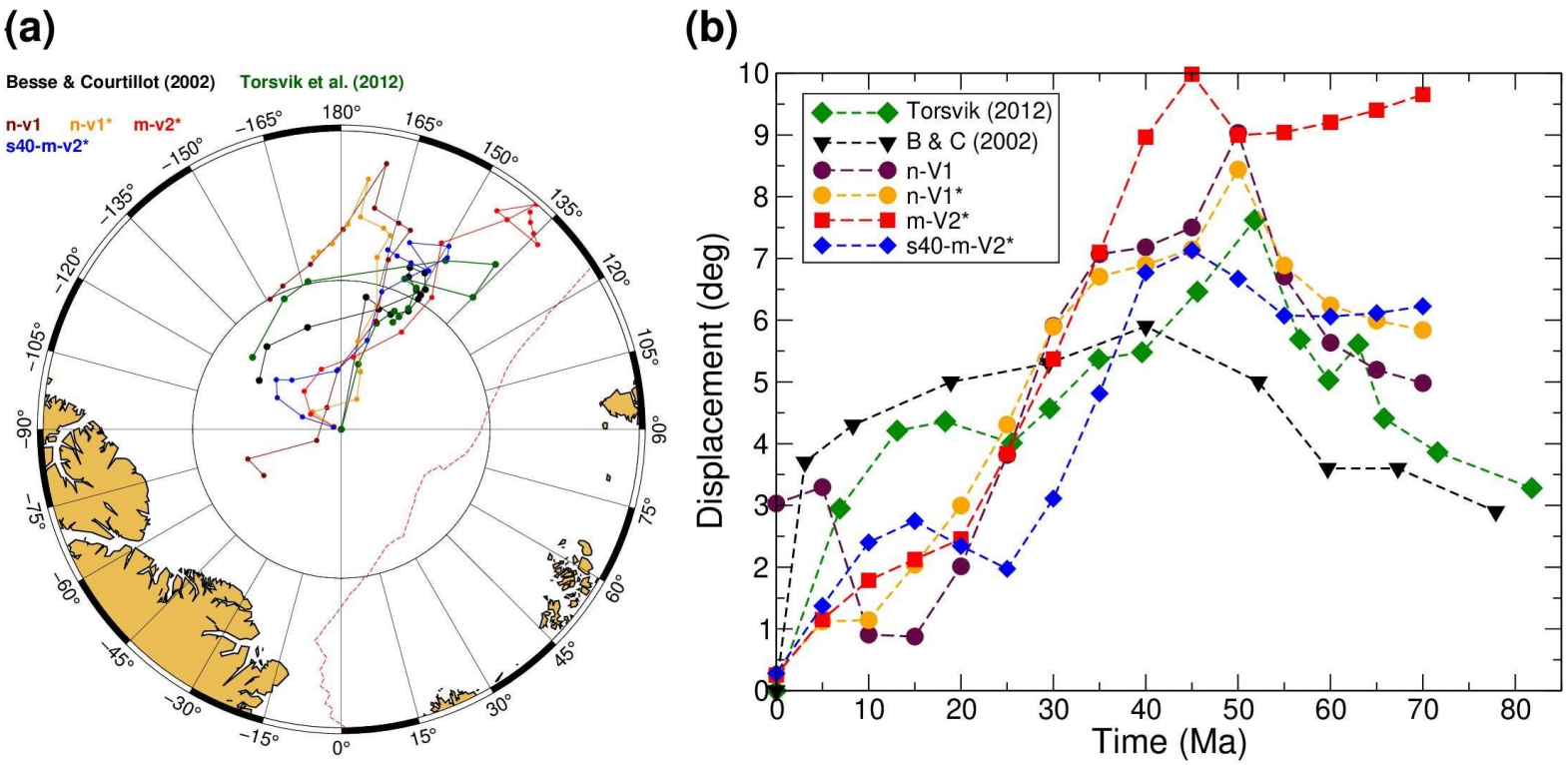

640

Figure 1: **Observed and predicted positions of Earth's rotation axis over geological time. (a)** The black curve represents a paleomagnetic estimate of TPW path determined by *Besse & Courtillot (2002)* in the Indo-Atlantic hotspot reference frame. The green curve represents the TPW path (see Table 1) that we estimate from the paleomagnetic data in *Torsvik et al. (2012)*, the global rotations of *Rowley et al. (2016)* and the *O'Neill et al. (2005)* rotations of plates relative to a fixed Indo-Atlantic hotspot frame. The colored curves represent the predicted TPW paths from 70-millionyear reconstructions of the mantle for convection models that employ either of two viscosity models (V1 and V2 – see Fig. S1) and two different tomography models (GyPSuM and S40RTS) as initial conditions (see Table 2): GyPSuM + V1 ('n-V1', maroon curve), GyPSuM + V1 ('n-V1*', orange curve), GyPSuM + V2 ('m-V2*', red curve), S40RTS + V2 ('s40-m-V2*', blue curve). The asterisk, *, identifies the predicted TPW paths obtained using a differential representation of the temporal changes in the moment of inertia (see equation 1 in *Methods*). No asterisk indicates the 'direct' representation (see equation 2 in *Methods*). Predictions marked with "m-" represent convection reconstructions where mantle flow is constrained to match geological reconstructions of past plate motions. Predictions marked with "n" do not impose this constraint. **(b)** Angular displacement of Earth's rotation poles relative to the present-day North Pole as a function of time (in millions of years, Ma). The figure compares predictions from different mantle viscosity profiles (V1 and V2) and initial tomography models (GyPSuM and S40RTS) described in panel (a), and in Table 2, with paleomagnetic data from *Torsvik et al. (2012)* and from *Besse & Courtillot (2002)*.The U-turn at 50 Ma, determined from both the *Torsvik et al. (2012)* data and from the V1 model predictions, represents the maximum deviation of the rotation pole from its present-day position.

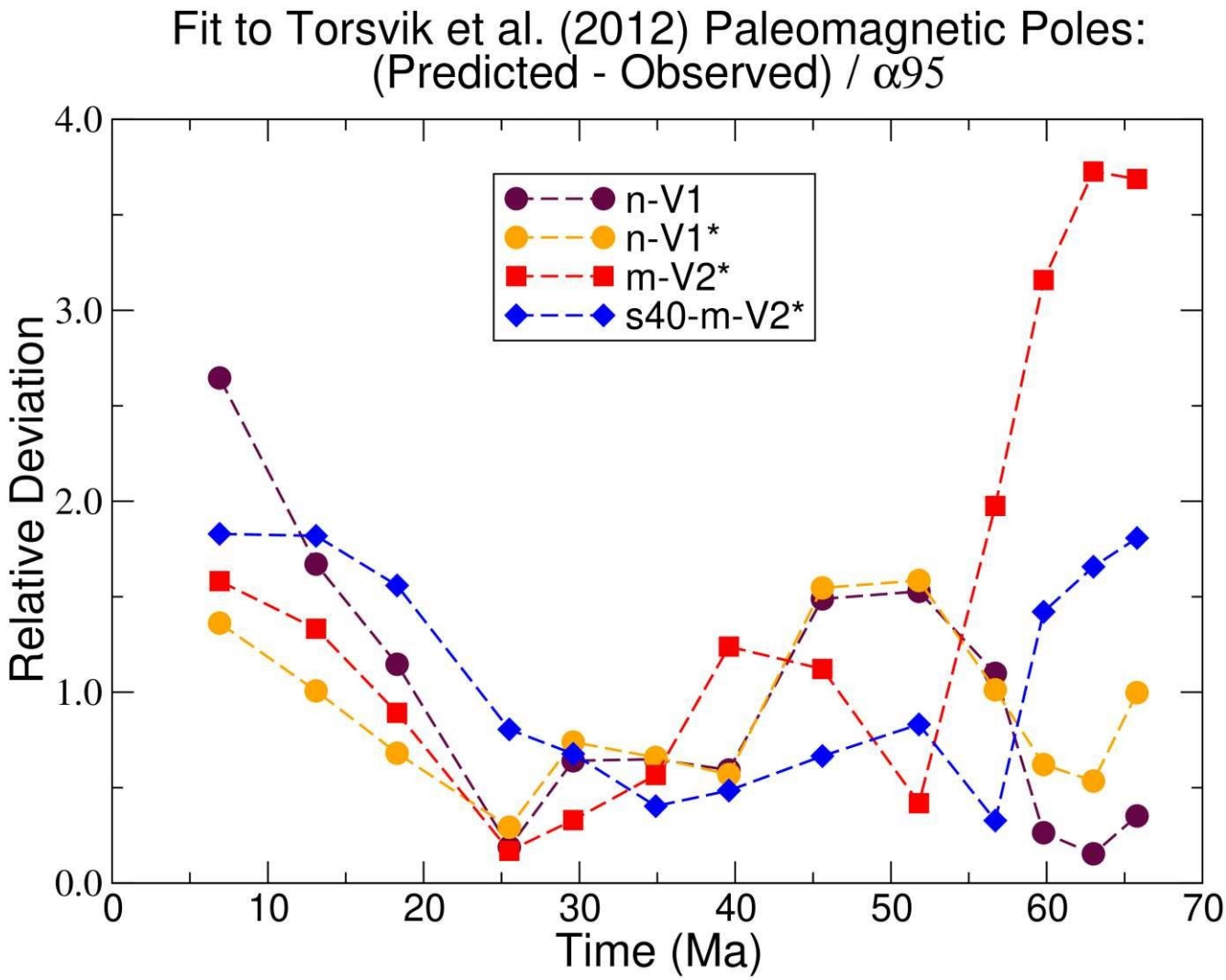

Figure 2: **Relative deviation between the predicted and observed positions of Earth's rotation pole** (in Fig. 1) as a function of time (in millions of years, Ma). The relative deviation is calculated as the angular distance between the predicted and observed pole positions, divided by the alpha-95 (α95) confidence interval (in Table 1). A relative deviation of less than or equal to 1 indicates that the predicted pole position falls within the α95 region, signifying an acceptable (good) fit. The different curves represent predictions (see Fig. 1 and its caption) based on two mantle viscosity profiles (V1 and V2) and two tomography models (GyPSuM and S40RTS).

641

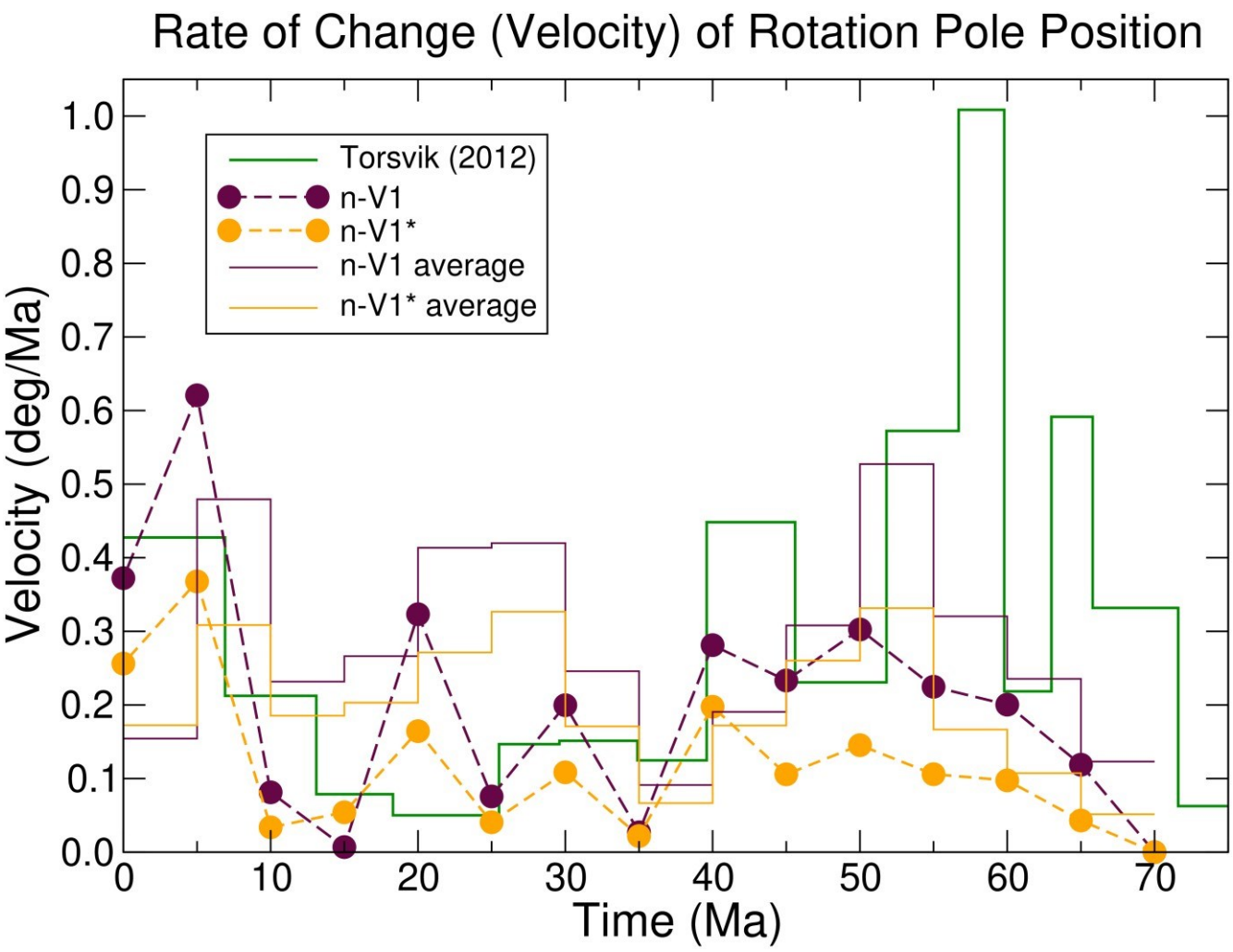

Figure 3: **Predicted and observed angular velocities of true polar wander (TPW) over the past 70 million years.** The green solid curve represents the interval-averaged rate of change of the rotation pole position based on the observed TPW path (Table 1), calculated from the paleomagnetic data of *Torsvik et al. (2012)*. Average angular velocities are computed by dividing the angular distance between successive pole positions by the elapsed time. The maroon solid curve shows the interval-averaged TPW velocity predicted by the n-V1 model using the direct approach for the moment of inertia perturbation (eq. 2 in *Methods*), averaged over 5-million-year intervals. The maroon dashed curve represents the instantaneous angular velocity of TPW for the n-V1 model, computed using equation (23) in the Supplementary Information. The orange solid and dashed curves show the interval-averaged and instantaneous TPW velocities, respectively, predicted by the n-V1* model using the differential approach for the moment of inertia perturbation (eq. 1 in *Methods*). The peak between 60 and 50 Ma in both the observed and predicted TPW velocities corresponds to the U-turn in the TPW path seen in Figure 1, reflecting a rapid change in the rotation pole's direction during this time. Note: 1°/Ma = 11 cm/year.

642

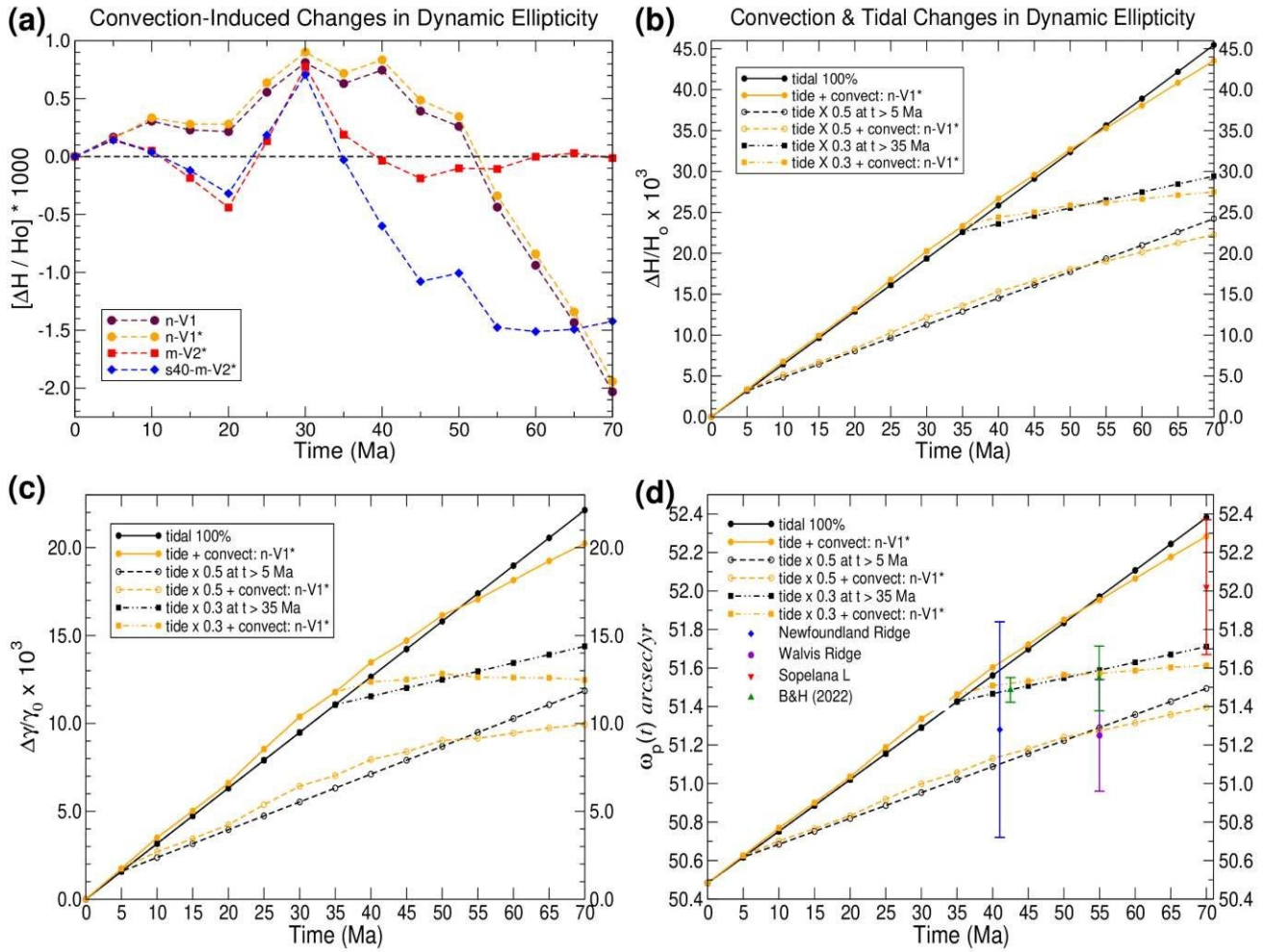

Figure 4: **Mantle-convection and tidally induced changes of Earth's dynamic flattening (ellipticity) and precession frequency over the past 70 million years**. **(a)** Change in dynamic flattening $\Delta H(t)/H_0$ as a function of time (in millions of years, Ma) relative to its present day (PD) value H_0, where $\Delta H(t) = H(t) - H_0$. The curves represent predictions (see Fig. 1 and its caption) based on different mantle viscosity profiles (V1 and V2) and tomography models (GyPSuM and S40RTS). Positive values indicate an increase in the flattening compared to PD, while negative values indicate a decrease. This evolution represents the contribution of mantle convection to Earth's precessional dynamics (see eq. 6 in *Methods*). **(b)** Combined effect of convection and tidally driven deceleration of rotation on dynamic flattening changes (see *Methods*, discussion following eq. 5). The solid black line ('tidal 100%') represents the prediction assuming PD tidal dissipation, given by the La2004 solution (see discussion in main text), is constant over past 70 Ma, and no changes due to mantle convection are included. The solid orange line represents the combined effect of TD and convection, where the latter is predicted for the n-V1* model – see orange curve in (a). Dashed lines show effect of reducing TD to 50% of PD for times earlier than 5 Ma, in absence of convection changes (black curve) and with convection (orange curve). Dashed-dotted lines represent the effect of reducing TD to 30% of PD for times earlier than 35 Ma, without (black curve) and with (orange) convection induced changes. **(c)** Change in flattening ratio, $\Delta\gamma(t)/\gamma_0$ where $\gamma = H\,\Omega/$ and $\Delta\gamma(t) = \gamma(t) - \gamma_0$. The curves represent the same models identified in (b). In all cases the black curves represent the effect of TD alone, while the orange curves represent combined TD and convection effects, where the latter is derived from the n-V1* convection model. **(d)** Changes in precession frequency, ω_{prec} (see equation 6 in *Methods*), over the past 70 Ma. The curves again represent the same models identified in (b) and (c). Observational estimates of ω_{prec} are also shown and they are labelled as: (i) 'Newfoundland Ridge' datum (blue diamond), from cyclostratigraphic analysis by *De*

Vleeschouwer et al. (*2023*), (ii) 'Walvis Ridge' (violet circle) and 'Sopelana L' (red triangle) data, compiled by *Wu et al.* (*2024*, see their Table 1), (iii) 'B&H (2022)' data (green triangles), from cyclostratigraphic analysis by Boulila & Hinnov (*2022*, see their Tables 3 & 4). The corresponding vertical bars represent the standard deviation.

644

645 Supplementary Information for

646 **Validating 70 Million Years of Convection Driven True Polar Wander and**
647 **Dynamic**

648 **Flattening with Paleomagnetic Data**

649 Alessandro Forte*, Petar Glišović, David Rowley, Marianne Greff, Shayan Kamali Lima

650 *Corresponding author. Email: forte@ufl.edu, forte@ipgp.fr

651

652 **This PDF file includes:**

653 Materials and Methods

654

Materials and Methods

1. Mantle Viscosity

Our back-and-forth iterative method for time-reversed convection modelling incorporates depth-dependent mantle viscosity. This input is critical for ensuring that the temporal evolution of mantle buoyancy occurs on time scales that are as Earth like as possible. Our convection modelling thus incorporates two depth-dependent, horizontally averaged, viscosity profiles ('V1' and 'V2', see Fig. S1) derived from joint inversions of convection-related global observables, such as plate velocities, gravity anomalies, crust-corrected dynamic topography, and core-mantle boundary ellipticity. Additionally, these viscosity profiles integrate ice-age geodynamic data associated with glacial isostatic adjustment (GIA), notably, the Fennoscandian relaxation spectrum and decay times determined from the postglacial sea level history in Hudson Bay and Sweden (*Mitrovica & Forte 2004*; *Forte et al. 2010*).

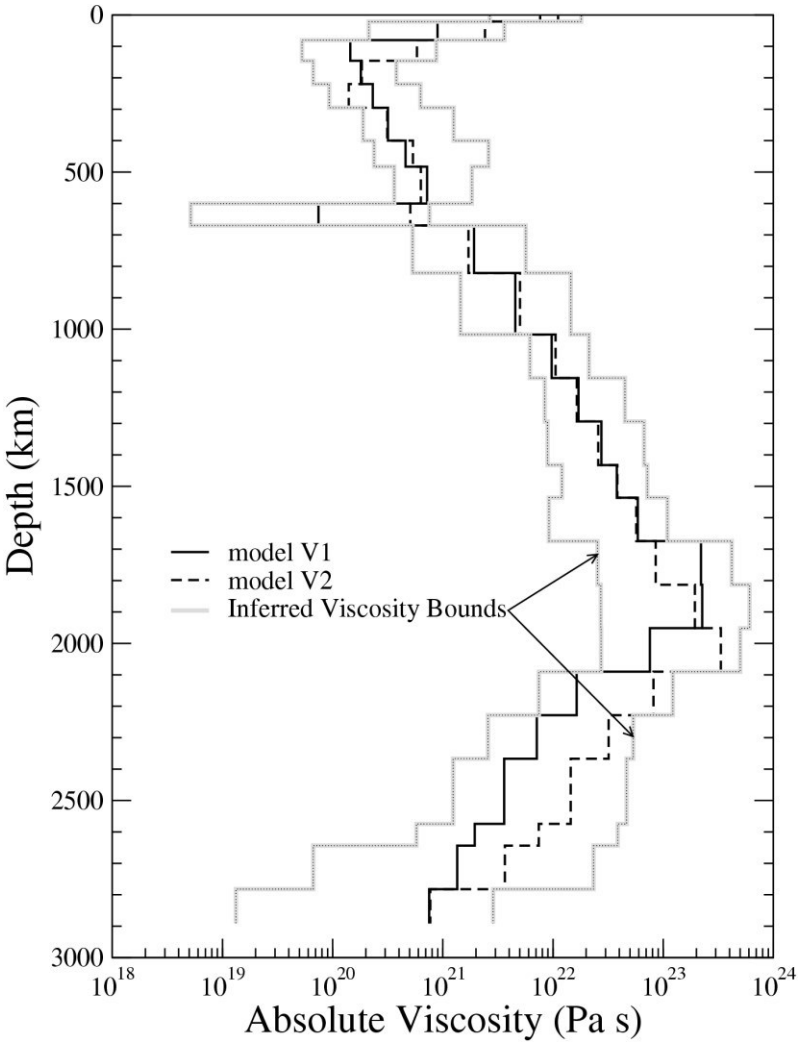

Figure S1: **Mantle viscosity inferrences from joint inversions of GIA and convection data sets**. The solid black line (model V1) is the viscosity profile that provides an optimal fit to the entire suite of geodynamic data (*Mitrovica and Forte 2004*). The dashed line (model V2) was inverted with strong smoothing constraints applied across the horizon separating upper and lower mantle and yields slightly lower fits to the combined GIA– convection data sets (*Forte et al., 2010*). The thick gray lines illustrate the range of allowable values of mantle viscosity, which are consistent with the joint GIA–convection constraints. Full details of the iterative, Occam-style inversion methodology are presented in *Mitrovica and Forte (2004)*.

665

666

667 **2. Degree-2 Geopotential and Earth's Moments of Inertia**

668 The spherical harmonic expansion of Earth's time-variable external gravitational potential field, $U(\vec{r}, t)$, in a 669 coordinate system whose origin coincides with Earth's centre of mass, is:

670
$$U(r,\theta,\varphi,t) = \frac{GM}{r}\left[1 + \sum_{l=2}^{\infty}\sum_{m=-l}^{l} U_l^m(t)\left(\frac{r_E}{r}\right)^l Y_l^m(\theta,\varphi)\right] \quad (1)$$

671 where M is the total mass of the Earth, G is the universal constant of gravitation, r_E is the mean radius of the Earth, 672 (r,θ,φ) respectively represent the radius, colatitude and longitude of any external point at position $\vec{r}$, t represents

673 time, $U_l^m(t)$ are the dimensionless time-dependent harmonic coefficients of the external geopotential, and 674 $Y_l^m(\theta,$ $\varphi)$ are complex spherical harmonics whose mean-square amplitude on the unit-radius sphere is unity:

675 $$\frac{1}{4\pi}\iint Y_l^m(\theta,\varphi)\, Y_{lm'}{}^*(\theta,\varphi)\sin\theta\, d\theta\, d\varphi = \delta_{l,l'}\,\delta_{m,m'}$$

676 where * denotes complex conjugation and $\delta_{i,j}$ represents the Kronecker delta equal to 1 when $i = j$ and equal to

677 0 otherwise.

678 The time-variable, 2nd-order moment of inertia tensor is defined by:

679 $$I_{i,j}(t) = \iiint [x_k x_k \delta_{i,j} - x_i x_j]\, \rho(\vec{r}, t)\sin\theta\, d\theta\, d\varphi\, r^2 dr \qquad (2)$$

680 where x_i $(i = 1,2,3)$ represent the (x, y, z) Cartesian coordinates of any point $\vec{r}$ inside the Earth, $\rho(\vec{r},t)$ is the 681 time-dependent mass density distribution inside the Earth, and the integration in (2) is carried out over the entire 682 volume of the Earth.

683 In our work, the time-dependence of the internal mass density arises from mantle convection:

684 $$\rho(\vec{r},t) = \rho_0(r, t) + \delta\rho(\vec{r}, t)\,, \qquad (3)$$

685 where $\rho_0(r, t)$ is the purely radial density distribution. In our calculations we assume that $\rho_0(r, t = 0)$ is given,

686 by the PREM reference Earth model (*Dziewonski & Anderson 1981*), and $\delta\rho(\vec{r},$ $t)$ are time-dependent density 687 perturbations generated by mantle convection whose horizontal average, at all depths, is equal to zero. We note

688 here that secular cooling due to mantle convection will also contribute to the time dependence of the radial density
689 distribution, $\rho_0(r, t)$. Substituting (3) into (2), we obtain the following expression for the reference moment of

690 inertia due to the radially symmetric $(l = 0)$ density distribution:

691 $$I_{i,j}{}^0(t) = I_0(t)\,\delta_{i,j}, \quad \text{where} \quad I_0(t) = \frac{8\pi}{3}\int_0^{r_E} \rho_0(r,t)\, r^4\, dr \qquad (4a)$$

692 and the following expression for the perturbations to the moment of inertia tensor generated by mantle convection:

$$\delta I_{i,j}^{\text{con}}(t) = \iiint [x_k x_k \delta_{i,j} - x_i x_j]\, \delta\rho(\vec{r},t)\, \sin\theta\, d\theta\, d\varphi\, r^2 dr \qquad (4b)$$

We underline here that expressions (4a-b) describe the moment of inertia for a spherical, non-rotating Earth. There will be additional contributions on a rotating Earth due to the centrifugal deformation, described in the next section below.

The effect of secular cooling on the scalar moment of inertia $I_0(t)$ in (4a) was assessed by *Greff-Lefftz* (*2011*), who determined that the largest contribution to the changes in $I_0(t)$ will be from the secular contraction of Earth's mean radius and then estimated that:

$$\frac{1}{I_0}\frac{dI_0}{dt} \cong -2 \times 10^{-3}\ \text{Ga}^{-1}$$

assuming a secular cooling rate of 100 K/Ga. For the time interval considered here (i.e., the past 70 Ma) the cooling-induced change in $I_0(t)$ will therefore be $\Delta I_0 \sim -0.14‰$. This is a negligibly small perturbation, and we therefore treat $I_0(t) = I_0(0) \equiv$ constant in our work.

Using the integral solution to the gravitational Poisson equation, one can establish a direct relationship between the convection-induced contributions to the degree $l = 2$ harmonic coefficients of Earth's external gravity potential in (1) and the individual components of the convection-induced perturbations of the moment of inertia tensor in (4):

$$\delta I_{x,x}^{\text{con}}(t) = \sqrt{5}\, r_e^2\, M \left[\frac{1}{3}\delta R_2^0(t) - \sqrt{\frac{2}{3}}\, \delta R_2^2(t)\right], \qquad (5a)$$

$$\delta I_{y,y}^{\text{con}}(t) = \sqrt{5}\, r_e^2\, M \left[\frac{1}{3}\delta R_2^0(t) + \sqrt{\frac{2}{3}}\, \delta R_2^2(t)\right], \qquad (5b)$$

$$\delta I_{z,z}^{\text{con}}(t) = \sqrt{5}\, r_e^2\, M \left[-\frac{2}{3}\delta R_2^0(t)\right], \qquad (5c)$$

$$\delta I_{x,y}^{\text{con}}(t) = \sqrt{5}\, r_e^2\, M \left[\sqrt{\frac{2}{3}}\, \delta I_2^2(t)\right], \qquad (5d)$$

$$\delta I_{x,z}^{\text{con}}(t) = \sqrt{5}\, r_e^2\, M \left[\sqrt{\frac{2}{3}}\, \delta R_2^1(t)\right], \qquad (5e)$$

$$\delta I_{y,z}^{\text{con}}(t) = \sqrt{5}\, r_e^2\, M \left[-\sqrt{\frac{2}{3}}\, \delta I_2^1(t)\right], \quad (5f)$$

where $\delta R_2^m(t) = Re[\,\delta U_2^m(t)]$, $\delta I_2^m(t) = Im[\,\delta U_2^m(t)]$, (5g)

and $\delta U_2^m(t)$ represent the convection-induced contributions to the degree-2 geopotential coefficients in (1).

From Brun's formula, the relationship between the convection-induced perturbations of the geopotential, described by harmonic coefficients $\delta U_l^m(t)$, and the corresponding undulations of the non-hydrostatic geoid surface, described by harmonic coefficients, $\delta N_l^m(t)$, relative to the reference hydrostatic ellipsoid with mean radius equal to r_E, is given by:

$$\delta N_l^m(t) = r_E\, \delta U_l^m(t) \quad (6)$$

Based on equation (6), we can now express all convection-induced perturbations of the moment of inertia tensor, in (5a-f), in terms of the convection-induced perturbations to Earth's geoid. This connection between moment of inertia and the geoid is of special utility because it allows the immediate application of the theoretical formulation of the viscous flow response of the mantle to internal density loads in terms of geodynamic kernel functions (*Richards & Hager 1984, Ricard et al. 1984, Forte & Peltier 1987*), as follows:

$$\delta N_l^m(t) = \frac{3}{\bar{\rho}\,(2l+1)} \int_{r_{CMB}}^{r_s} G_l(\eta|r)\, \delta\rho_l^m(r,t)\, dr \quad (7)$$

where $\bar{\rho}$ is the mean density of the Earth, r_s is the mean radius of the solid surface of the Earth, r_{CMB} is the mean radius of the core-mantle boundary (CMB), and $G_l(\eta|r)$ is the harmonic degree-l geoid kernel calculated for a viscous, deformable mantle in which the explicit functional dependence on viscosity η is indicated, and $\delta\rho_l^m(r,t)$ are harmonic coefficients of the time-dependent internal

density anomalies generated by mantle convection. For 731 the work presented in the main text, we employed geoid kernels for a compressible, self-gravitating mantle that 732 are calculated for both the V1 and V2 radial viscosity profiles, for two different surface boundary conditions – no733 slip and free-slip – required to model the mechanical feedback of the tectonic plates on the underlying mantle flow

734 (for more details, see *Forte et al. 2015*).
735

736 **3. Angular Momentum of a Rotating Deformable Earth**

737 The moment of inertia on a rotating, deformable planet must also include the influence of the centrifugal potential 738 on the internal mass distribution and on the external gravitational figure. As described in *Ricard et al. (1993)*, the 739 total inertia tensor will then be given by the following expression:

$$I_{i,j}(t) = I_0\ \delta_{i,j} + \frac{3}{r^5}{}^{e}G\ k^{T}(t) * [\omega_i(t)\omega_j(t) - \frac{1}{3}\ \omega^2(t)\delta_{i,j}] + \delta I_{i,j}{}^{\mathrm{con}}(t) \quad (8)$$

741 Where I_0 is the scalar moment of inertia in (4a), $k^T(t)$ is the time-dependent tidal Love number, $\omega_i(t)$ is the *i*'th

742 Cartesian component of Earth's instantaneous rotation vector $\boldsymbol{\omega}(t)$, * denotes time convolution, and $\delta I_{i,j}{}^{\mathrm{con}}(t)$ is

743 the perturbation generated by the time-dependent mass redistribution generated by mantle convection.

744 For sufficiently long times, as was shown by *Ricard et al. (1993)*, the Maxwell viscoelastic behaviour of Earth's

745 deformation can be approximated, in the Laplace transform domain, by the following expression for the tidal Love

746 number:

747 $$k^T(s, LT) \cong k_f{}^T(LT)\ [\,1 - T_1\, s\,] \quad (9)$$

748 where s is the Laplace transform variable, LT is the long-term ($t \to \infty$) elastic lithosphere thickness, $k_f{}^T(LT)$ is

749 the fluid tidal Love number that depends on the elastic thickness of the lithosphere, and T_1 (> 0) is a time constant 750 that depends on the depth-dependence of viscosity and density. Transforming (9) to the time domain then yields:

751 $k^T(t, LT) \cong k_f{}^T(LT)[\,\delta(t) - T_1\,\dot{\delta}(t)]$ (10) 752 where $\delta(t)$ is the Dirac delta function and the overdot denotes the time derivative.

753 The hypothesized long-term 'remnant bulge' that stabilizes a planet's rotational behaviour, presented in 754 *Matsuyama et al. (2006)*, was further employed by *Creveling et al. (2012)* and *Chan et al. (2014)* who modelled 755 an additional contribution to Earth's moment of inertia arising from this remnant rotational bulge, given by the 756 following expression:

757 $\delta I_{i,j\text{bulge}}(t) = \frac{e}{} \left[k^{*T}_f - k^T_f(LT) \right]_{3rG5} \quad \Omega_{2i} \quad (\delta_{i,3} - \_ \quad 13) \quad \delta_{i,j}$ (11)

758 in which $k^*{}_f{}^T$ is the fluid tidal Love number for a purely hydrostatic Earth (i.e., $k^*{}_f{}^T = k_f{}^T(LT = 0)$) and Ω_i is

759 the initial angular velocity associated with the formation of the remnant bulge (*Matsuyama et al. 2006*). It is 760 important to note that the Einstein tensor summation convention is suspended in (11) (and in all subsequent

761 expressions involving $\delta I_{i,j}{}^{\text{bulge}}$) and there should be no summation over the index i. The Earth's total moment of 762 inertia is then obtained by adding the remnant bulge contribution in (11) to that in (8), yielding:

763 $$I_{i,j}(t) = I_0\,\delta_{i,j} + 3\frac{r_5}{}{}_e G\,k_T(t, LT) * [\omega_i(t)\omega_j(t) - \_13\,\omega_2(t)\delta_{i,j}] + \delta I_{i,j\text{bulge}}(t) + \delta I_{i,j\text{con}}(t)$$

764 and after substituting (10) into the above expression and working out the temporal convolution, we finally obtain:

765 $$I_{i,j}(t) = I_0\,\delta_{i,j} + \frac{r^5}{}{}3^e G\,k_f{}^T(LT)\{\,[\omega_i(t)\omega_j(t) - \_13\,\omega^2(t)\delta_{i,j}]$$

$$- T_1 [\dot{\omega}_i(t)\omega_j(t) + \omega_i(t)\dot{\omega}_j(t) - \frac{2}{3}\dot{\omega}_k(t)\omega_k(t)\,\delta_{i,j}] \}$$

$$\frac{r^5}{3G}\left[k^{*T}_f - k^T_f(LT) \right] \omega_{2i}\,(\delta_{i,3} - \tfrac{1}{3})\,\delta_{i,j} + \delta I_{i,j}^{\text{con}}(t) \quad (12)$$

We now determine Earth's time-dependent angular momentum vector:

$$\mathrm{L}(t) = \underline{\boldsymbol{I}}(t) \cdot \boldsymbol{\omega}(t) = I_{i,j}(t)\,\omega_j(t)\,\hat{\boldsymbol{e}}_{\boldsymbol{i}} \quad (13)$$

where $\hat{\boldsymbol{e}}_{\boldsymbol{i}}$ is the unit basis vector on the *i*'th axis in a Cartesian coordinate system. Substituting (12) into (13) finally yields the expression for the angular momentum of a rotating, deformable Earth perturbed by mantle convection:

$$\mathrm{L}(t) = [\, I_0 + \frac{r^5}{3}\,{}^{e}G\,k_f{}^{T}(LT)\,\{\tfrac{2}{3}\omega^2(t) - T_1 3^{1}\dot{\omega}_k(t)\omega_k\}\,]\,\boldsymbol{\omega}(t) -$$

$$[\, \frac{r^5}{3}\,{}^{e}G\,k_f{}^{T}(LT)\,\omega^2(t)\,T_1\,]\,\boldsymbol{\dot{\omega}}\,(t) + \delta I^{S}_{i,j}(t)\,\omega_j(t)\,\hat{\boldsymbol{e}}_{\boldsymbol{i}} \quad (14)$$

in which we defined a so-called "stabilized" moment of inertia perturbation:

$$\delta I^{S}_{i,j}(t) = \delta I_{i,j}^{\text{con}}(t) + \left(\frac{{}^{e}3\,\Omega_G{}^{2i}\,k^{*}{}_f{}^{T}}{r^5}\right)[1 - k^{f}_{T}\,k^T(_{*}LT_{fT})]\,(\delta_{i,3} - \tfrac{1}{3})\,\delta_{i,j} \quad (15)$$

Following *Munk and MacDonald (1960)*, the first factor appearing in the remnant bulge stabilization in (15) may be directly related to the dynamical flattening as follows:

$$\frac{r^5}{3G}\,{}^{e}\Omega_{2i}\,k_{*fT} = (C - A)^{\text{hydro}}$$

where $(C - A)^{\text{hydro}}$ is the difference between maximum (polar) and minimum (equatorial) moments of inertia of a purely hydrostatic planet with angular velocity Ω_i.

4. Rotational Dynamics on a Deformable Earth

We begin with the Euler equation of conservation of angular momentum, without external torques, in a body-fixed rotating reference frame *(Goldstein 1980)*:

$$\frac{d\mathrm{L}}{dt} + \boldsymbol{\omega} \times \mathrm{L} = 0 \qquad (16)$$

where $\boldsymbol{\omega}$ is the angular velocity of the Earth. As argued by *Ricard et al. (1993)* and *Greff-Lefftz (2011)*,

$$\frac{d\mathrm{L}}{dt} \ll \boldsymbol{\omega} \times \mathrm{L}$$

because the long-time scale, convection-induced changes in $\mathrm{L}(t)$ are orders of magnitude slower than the diurnal time scale associated with $\boldsymbol{\omega}(t)$. This 'quasistatic' approximation, where

$$\frac{d\mathrm{L}}{dt} \cong 0$$

requires that $\|\boldsymbol{\omega}(t)\| = \Omega = \text{constant}$, namely that the length of day is constant (*Greff-Lefftz 2011*). Returning to (16), the quasistatic approximation applicable to mantle-convection induced changes in Earth's angular momentum is:

$$\boldsymbol{\omega}(t) \times \mathrm{L}(t) = 0 \quad \text{and} \quad \|\boldsymbol{\omega}(t)\|^2 = \Omega^2 \qquad (17)$$

The substitution of expression (14), for Earth's total angular momentum, into the quasistatic approximation (17) for conservation of angular momentum yields:

797 $$\boldsymbol{\omega}(t) \times \{ - [\, 3^{r_e} G^5 \, k_f{}^T (LT)\, \Omega^2\, T_1 \,]\, \dot{\boldsymbol{\omega}}\,(t) + \delta I^S{}_{i,j}(t)\, \omega_j(t)\, \hat{\boldsymbol{e}}_i \} = 0 \qquad (18)$$

798 Expression (18) can be identically satisfied if the terms appearing in curly braces are colinear with the rotation 799 vector $\boldsymbol{\omega}(t)$:

800 $$- [\, 3^{r_e} G^5 \, k_f{}^T (LT)\, \Omega^2\, T_1 \,]\, \dot{\boldsymbol{\omega}}\,(t) + \delta I^S{}_{i,j}(t)\, \omega_j(t)\, \hat{\boldsymbol{e}}_i = \lambda\, \boldsymbol{\omega}(t) \qquad (19)$$

801 Equation (19) shows that when $\dot{\boldsymbol{\omega}}\,(t) = 0$, then

802 $$\underline{\boldsymbol{\delta I}}^S(t) \cdot \boldsymbol{\omega}(t) = \lambda\, \boldsymbol{\omega}(t) \qquad (20)$$

803 Equation (20) is a classic eigenvalue problem that yields a solution for $\boldsymbol{\omega}(t)$ corresponding to Earth's 'equilibrium'

804 rotation axis, attained when the viscous adjustment of Earth's rotational bulge is very rapid (i.e., when $T_1 \to 0$). 805 We thus recognize that λ in (19) is a 'time-dependent eigenvalue' that satisfies (20) only for equilibrium rotation.

806 Equation (19) can be further extended by noting that the constant length-of-day constraint in (17) yields:

807 $$\frac{d\Omega^2}{dt} = 0 \Rightarrow \boldsymbol{\omega}(t) \cdot \dot{\boldsymbol{\omega}}\,(t) = 0 \qquad (21)$$

808 Given the orthogonality condition in (21), taking the dot product of both sides of expression (19) by $\boldsymbol{\omega}(t)\,\cdot$ yields 809 the following expression for the time-dependent 'eigenvalue': 810 $\lambda\,(t) = \hat{\boldsymbol{\omega}}(t) \cdot \underline{\boldsymbol{\delta I}}^S(t) \cdot \hat{\boldsymbol{\omega}}(t)$

, where $\hat{\boldsymbol{\omega}}(t) = \frac{\boldsymbol{\omega}(t)}{\Omega}$ (22)

811 We next substitute (22) into equation (19) to finally obtain:

812 $$\beta\, T_1\, \dot{\boldsymbol{\omega}}\,(t) = \left[\underline{\boldsymbol{\delta I}}^S(t) - \left\{\hat{\boldsymbol{\omega}}(t) \cdot \underline{\boldsymbol{\delta I}}^S(t) \cdot \hat{\boldsymbol{\omega}}(t)\right\} \underline{\boldsymbol{I}}\right] \cdot\, \boldsymbol{\omega}(t), \qquad (23a)$$

813 where $$\beta = 3^{r_e} G^5\, k_f{}^T (LT)\, \Omega^2 = (C - A)^{\text{hydro}} \frac{k_f T}{k_* LT_{fT}} \qquad (23b)$$

Equation (23a-b) is of fundamental importance, because it governs the time-dependent evolution of Earth's rotation vector, and hence the trajectory of the pole, in response to the time-dependent moment of inertia perturbations generated by mantle convection, which are themselves modulated by the delayed response due to the viscous adjustment of the rotational bulge and the stabilization arising from a remnant rotational bulge. We note that no assumption is made concerning how small or how large is the departure of the rotation pole from current North Pole, nor do we need to explicitly diagonalize the moment of inertia tensor to calculate the maximum moment of inertia and its corresponding eigenvector, which defines the equilibrium rotation pole. We further note that equation (23) was also derived in *Rose & Buffett (2017)*, who employed it in their investigation of scaling relationships for the rates of TPW expected on a convecting Earth.

In practice, in our modelling of TPW induced by mantle convection, we numerically integrate (23) using an accurate Bulirsch-Stoer algorithm for solving systems of first-order differential equations (*Press et al. 2007*).

5. Remnant Bulge Stabilization of TPW

Here we explicitly explore the magnitude of the stabilization of mantle-convection-induced TPW arising from the remnant rotational bulge described in equations (11) and (15). For this purpose, we consider the TPW predictions presented in the main text for the n-V1* convection model (see Figure 1 and Table 2), obtained using the GyPSuM

tomography model as an initial condition and using the V1 viscosity profile and the fluid tidal Love number $k_f{}^T(LT = 30$ km). The value $LT = 30$ km, chosen for all the TPW predictions presented in the main text, is motivated by the study of *Watts & Moore (2017)* who analyzed the impact of elastic lithosphere flexure on crustal isostatic contributions to the spectral amplitude of free-air gravity anomalies and concluded that the best match is obtained with a global mean thickness of $LT = 34$ km.

We now consider TPW predictions, using the same convection-induced changes to the mantle density distribution obtained with the n-V1 models (Figure 1), for two different values of the elastic thickness of the lithosphere: $LT = 10$ km and $LT = 0$ km. The TPW predictions obtained using $LT = 0$ km involve no remnant rotation bulge, as expected from equation (11). The value $LT = 10$ km was the preferred value employed in *Creveling et al. (2012)*. As shown in Figure S2, the predicted TPW, in particular its maximum angular displacement relative to the position of the present-day rotation pole (in Figure S2b), will be increasingly amplified – as expected – when the elastic thickness is progressively reduced to a value of zero. The peak difference, at 50 Ma, between the $LT = 30$ km and $LT = 0$ km TPW predictions is ~2 degrees for the n-V1* model.

We also find that for $LT = 0$ and 10 km, the goodness of fit measure $X_{TPW}{}^2$ (see equation 4 in *Methods*) is 1.60 and 1.34, respectively, compared to $X_{TPW}{}^2 = 0.95$ for $LT = 30$ km, where in each case we refer to the n-V1* predictions in Figure S2a. These results suggest that $LT = 30$ km provides a better fit to the paleomagnetic constraints on TPW, when interpreted in terms of the n-V1* convection model. As the elastic thickness is reduced to zero, the speed of TPW is increased, as might be anticipated (Figure S2c) although the impact on the predicted present-day rate of TPW is relatively small. Finally, as shown in Figure S2d, the impact of the remnant bulge on the predicted changes in dynamic flattening is quite small.

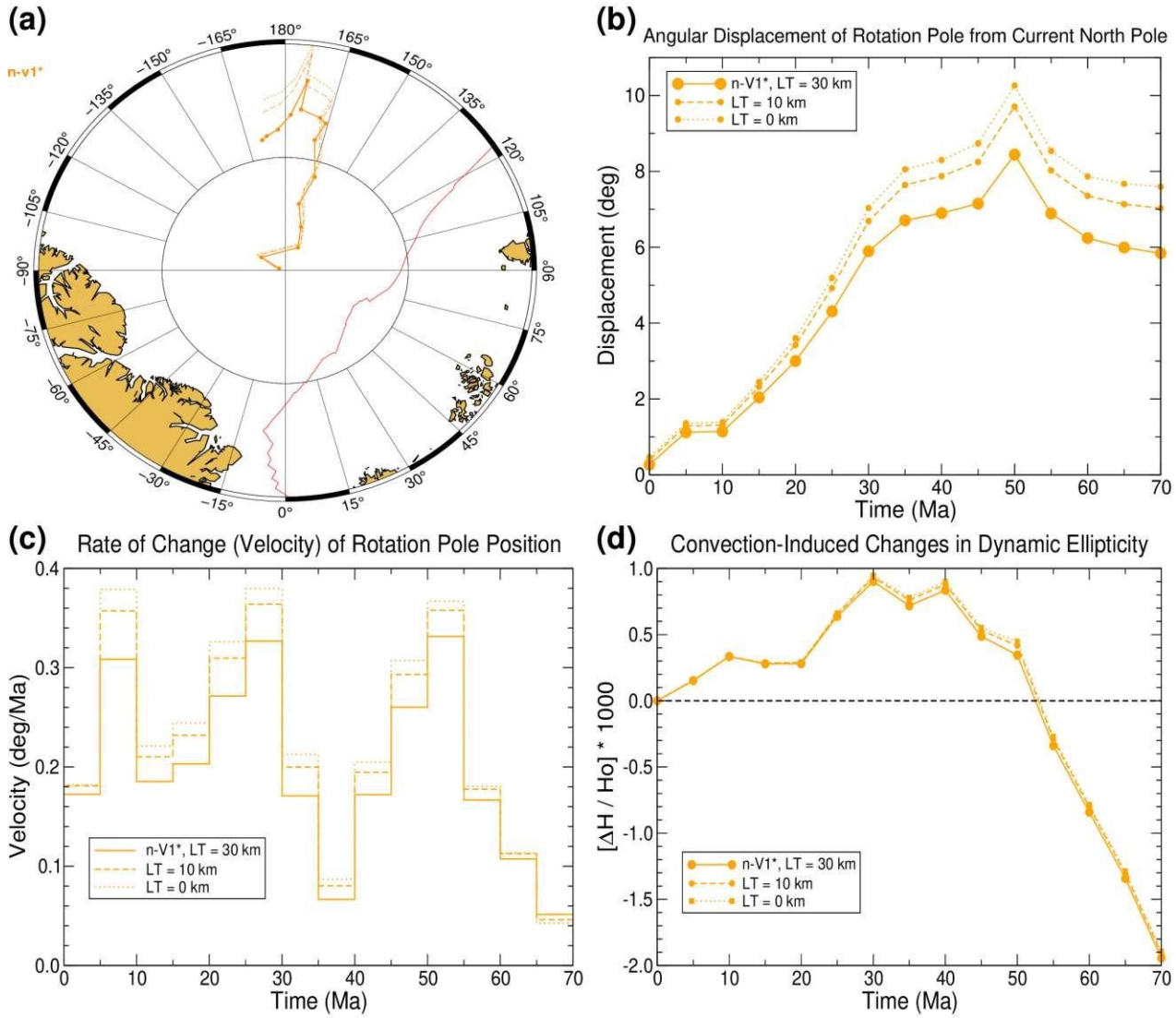

850

Figure S2: **Impact of the remnant rotational bulge on mantle-convection induced TPW. (a)** The curves represent predicted TPW paths assuming different values of the elastic thickness of the lithosphere that govern the remnant or fossil rotational bulge. The solid, dashed and dotted curves, here and in all subsequence panels (b to d), represent the TPW predicted assuming that the elastic thickness is $LT = 30{,}10{,}0\ km$, respectively. The paths of the rotation pole are predicted using 70-million-year reconstructions of the mantle for a convection model that employs viscosity model V1 (see Fig. S1) and the GyPSuM tomography model as an initial condition (see Table 2): GyPSuM + V1 = 'n-V1*'. The asterisk * identifies the predicted TPW paths obtained using a differential representation of the temporal changes in the moment of inertia (see equation 1 in *Methods*). The prefix "n-" denotes reconstructions where mantle flow is not constrained to match past plate motions. **(b)** Angular displacement of Earth's rotation poles relative to the present-day North Pole as a function of time (in millions of years, Ma) for the mantle convection predictions in (a). **(c)** Here are shown only the "average" angular velocities (not the transient, instantaneous velocities as in Fig. 3), which are computed by dividing the angular distance between successive pole positions by the elapsed time. In all cases, peak velocities are observed at 55 – 50 Ma, 30 – 25 Ma and 10 – 5 Ma. **(d)** This figure shows the corresponding changes in dynamic ellipticity ΔH as a function of time (in millions of years, Ma) relative to its present-day value H_0, where $\Delta H = H - H_0$. These changes determine the impact of mantle convection on Earth's precessional dynamics, as described in eq. 24.

6. Dynamic Ellipticity

As shown in *Goldstein (1980)* and *Stacey & Davis (2008)*, the average angular rate of astronomical precession, ω_{prec}, of Earth's rotation axis relative to the pole of Earth's ecliptic plane, due to the torque generated by the gravitational attraction of the Sun and Moon on Earth's rotational bulge, is given (to zeroth order accuracy – compare with equation (8) in *Laskar et al. 2004*) by the following expression:

$$\omega_{prec} = 2\,\overline{\Omega}\,\overline{[}\,\overline{a_{3S}} + \underset{S}{\overline{Gm_{a_{L3L}}}}]\cos\varepsilon \qquad (24)$$

in which Ω is Earth's diurnal rotation rate, M_S & m_L are the masses of the Sun and Moon, respectively, a_S & a_L are the corresponding average orbital distance (expressed in terms of the semi-major axis) between the Earth and the Sun and Moon, respectively, ε is the obliquity angle between Earth's axis of rotation and the axis perpendicular to the ecliptic plane, and H is Earth's dynamic ellipticity/flattening:

$$H(t) = \frac{C(t) - \frac{1}{2}[A(t) + B(t)]}{C(t)} \qquad (25)$$

in which

$$C(t) \geq B(t) \geq A(t) \qquad (26)$$

are the three principal moments (eigenvalues) of Earth's time-dependent moment of inertia tensor.

In past studies of geodynamic-induced perturbations to dynamic flattening (e.g., *Laskar et al., 1993, Forte & Mitrovica 1997, Ghelichkhan et al. 2021*), first-order perturbations of $H(t)$ described in (25) are determined, yielding the following expression:

869 $$\frac{\delta H}{H} = -\frac{3}{2}\frac{\delta C}{HC} \quad (27)$$

870 which is obtained assuming that $H(t) \ll 1$. If the U_2^1 (complex-valued) harmonic coefficient of Earth's

871 gravitational potential in equation (1) is zero or negligibly small, then the greatest moment of inertia C is given by 872 the following expression (*Chambat & Valette 2001*):

873 $$C = I^0 - \frac{2}{3}\sqrt{5}\, M r_E^2\, U_2^0 \quad (28)$$ 874 in which U_2^0 is the (real-valued) degree-2 zonal coefficient in Earth's geopotential (see equation 1). If we now 875 assume that some geodynamic process (e.g. mantle convection) perturbs Earth's gravity field, then from (28) we 876 obtain:

877 $$\delta C = \frac{2}{3}\sqrt{5}\, M r_E^2\, \delta U_2^0$$

878 and substitution into (27) yields:

879 $$\frac{\delta H M r^2}{HHC} = -\sqrt{5}\, r_E^2\, \delta U_2^0 \quad (29)$$

880 As noted above, equation (29) is obtained assuming that the U_2^1 geopotential coefficient is zero or negligibly small,

881 implying that the principal direction associated with largest moment, C, remains fixed to the z-axis of the 882 coordinate system. The latter assumption does not admit displacements of the rotation axis, and hence no TPW. In 883 all analyses of convection-induced changes to dynamic flattening presented in this work, we instead calculate the 884 following:

885 $$\frac{\Delta H(t)}{H_0} = \frac{H(t) - H_0}{H_0} \quad (30)$$

886 in which $H_0 = H(0)$ and $H(t)$ is always calculated, according to (25), from the eigenvalues of the complete time-

887 dependent moment of inertia tensor in (12), which incorporates the time-variable position of Earth's rotation axis

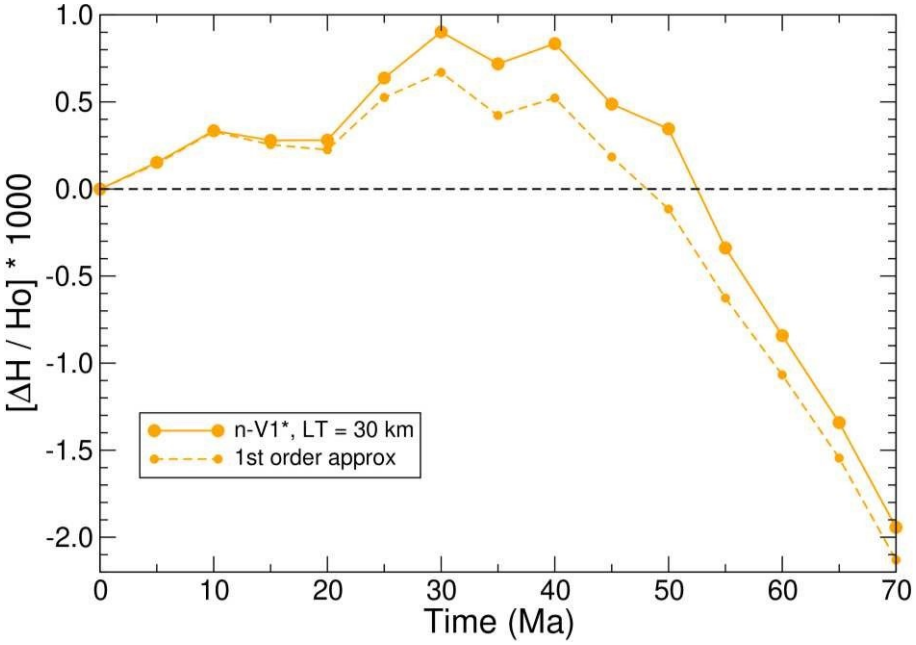

Figure S3: **Accuracy of the 1st order calculation of changes in dynamic flattening.** The dashed curve represents the predicted perturbation of dynamic ellipticity, $\delta H/H_0$, relative to the present-day value H_0, calculated using eq. (29). In this calculation we also employ the present-day value for the principal moment C. The solid curve represents the predicted $\Delta H/H_0$ calculated using eq. (30) and employing the complete timedependent moment of inertia tensor in eq. (12).

888 $\boldsymbol{\omega}(t)$ that is found in the TPW predictions presented in Figure 1 (main text) and Figure S2. The difference between
889 the 1st-order approximation (29) and the exact calculation (30) is illustrated here in Figure S3.
890
891 Equation (24) is an approximate expression that ignores the small (~5°) angle between the plane of the lunar orbit
892 relative to the ecliptic plane, the small eccentricity of the Earth and Moon orbit, and ignores the gravitational
893 impact of other planets on the evolution of Earth's orbit (for details see the many-body theory presented in *Laskar*
894 *et al. 1993,2004*). Equation (24) serves, however, to identify a critical linear relationship between the frequency
895 of precession ω_{prec} and the dynamic flattening $H(t)$, which remains true in the complete many-body theory (*Laskar*
896 *et al. 2004*). A frequency analysis of Earth's orbital evolution over the past 18 Ma, by *Laskar et al., 1993*, revealed
897 the dominant contribution from Earth's main precession frequency $\omega_{prec} = 50.4712$ arcsec/yr (corresponding to a
898 period of 25,678 yr) in addition to frequencies associated with quasi-periodic gravitational perturbations of other
899 planets on Earth's orbital evolution. The most significant of these quasi-periodic perturbations occurs at the
900 frequency $f = s_6 - g_6 + g_5 = 50.3017$ arcsec/yr, where g_5 and g_6 are the secular frequencies related to the
901 perihelion of Jupiter and Saturn, respectively and s_6 is related to the node of Saturn (*Laskar et al. 1993*).
902 As discussed in *Laskar et al.* (*1993*), and following from equation (24), any geodynamic process that reduces the
903 dynamic flattening $H(t)$ by at least -0.2% will then drive the main precession frequency ω_{prec} towards the
904 frequency f associated with the quasi-periodic perturbations by Jupiter and Saturn, leading to a resonance that
905 significantly perturbs the temporal evolution of Earth's orbital parameters (i.e., the obliquity angle and precession
906 frequency) and hence will modify the Milankovitch insolation cycles. As discussed in *Laskar et al. (2004)* this
907 resonance is predicted to occur in the next few million years, owing to the continuing reduction of $H(t)$ and
908 increase in Earth-Moon distance a_L, due to tidal-induced deceleration of Earth's rotation rate. The possibility that
909 this resonance crossing may have occurred in the past was explored by *Forte & Mitrovica* (*1997*) who suggested
910 that mantle-convection induced changes to $H(t)$, over the past 20 Ma, were large enough to generate such a passage
911 through resonance. However, *Morrow et al.* (*2012*) subsequently examined the combined effects of glacial isostatic
912 adjustment (GIA) and mantle convection over the past 25 Ma and found more modest time-averaged

914 changes to $H(t)$ and that these changes were not easily reconciled with independent cyclo-stratigraphic 915 constraints. This lack of reconciliation raised an "enigma" concerning the link between observational constraints

916 on $H(t)$ changes and the current understanding of the fundamental geodynamic processes that drive these changes.

917 These issues, including the above enigma, are ultimately dependent on a rigorous and accurate determination of

918 the present-day value of dynamic ellipticity, $H_0 = H(t = 0)$, since this determines the starting, baseline-value for

919 relative changes in dynamic ellipticity, defined in (30), and – critically – the baseline-value for the present-

day 920 rate of precession $\omega_{prec}(t = 0)$ in (24). These points are treated in detail below (in section 7).

921

922 **7. Hydrostatic Flattening: Impact of Tidal Deceleration**

923 Our preceding consideration, related to equation (28), of the importance of the principal (polar) moment of inertia,

924 C, for understanding changes in Earth's dynamic flattening (embodied in equation 27) motivates the following 925 review of some fundamental notions concerning the hydrostatic equilibrium of a rotating planet. This will set the 926 stage for a quantitative assessment of the impact of secular changes of Earth's diurnal rate of rotation (i.e., the 927 length of day) due to long-term tidal friction that is needed for the results presented in Figure 4b (main text) and 928 related discussion.

929 In the absence of TPW, and with no internal dynamics, Earth's angular rotation vector is $\boldsymbol{\omega} = \Omega\hat{\boldsymbol{z}}$ and $\delta I_{i,j}^{\text{con}}(t) = 930$

0. From equation (12) we thus obtain the following expressions for the moment of inertia tensor:

931 $$I_{xx} = \frac{1}{3}(LT) - \frac{r_e^5}{\Omega G}\frac{\Omega^2}{2}\left[k_f^{*T} - k_f^T(LT)\right] \quad I_{yy} = I_0 - \frac{1}{3}\frac{r_e^5}{\Omega G}\frac{\Omega^2}{2}\left[\right.$$

932 $$0 \quad \frac{1}{3}I = \frac{r^5}{3G}(31a) + \frac{1}{3}\frac{r_e^5(\Omega_i^2 - \Omega^2)}{3G}k_f^T(LT) \quad {}^{e}\Omega^{2i}\,k^{*}{}_f{}^T$$

$$zz \quad {}_0 3 \quad \frac{2r^5}{3G} \quad 3 \quad \frac{3}{3G} \quad f \quad {}_f 933 \quad I = I + \frac{}{}{}_e\Omega_2\, k_T(LT) + \frac{}{}2\, r_{e5}\,\Omega_{2i}\,[$$

$$k_{*T} - k_T(LT)\,]$$

934 $$0 \quad \frac{2r^5}{3} = I \quad -\frac{2}{3}\frac{r_e^5(\Omega_i^2 - \Omega^2)}{3G} k_f^T(LT) + {}^{e}\Omega^{2i} k^{*}{}_f{}^T \quad (31b)$$

935 $$I_{xy} = I_{xz} = I_{yz} = 0 \quad (31c)$$

936 The expression describing the external gravitational potential of a rotating hydrostatic Earth with no internal mass

937 anomalies is, to 2nd-order accuracy (*Chambat et al. 2010*), given by:

938 $$U^{hyd}(r,\theta) = \frac{GM}{r}\left[1 - \bar{J}_2^{hyd}\left(\frac{a}{r^E}\right)^2 P_2(\cos\theta) - \bar{J}_4^{hyd}\left(\frac{a}{r^E}\right)^4 P_4(\cos\theta)\right] \quad (32a)$$

939 where $\bar{\bar{J}}_{nhyd}(n = 2,4, \ldots)$ are nondimensional gravitational form coefficients for a hydrostatic planet, $P_n(\cos\theta)$ are

940 the corresponding Legendre polynomials of degree n, and a_E is the equatorial radius of the reference ellipsoid.

941 The geopotential expansion in (1) has been defined with respect to

the mean radius of the Earth, r_E and, in the 942 interest of

consistency, we then rewrite (32a) as follows:

943 $$U^{hyd}(r,\theta) = \frac{GM}{r}\left[1 - J_2^{hyd}\left(\frac{r}{r^E}\right)^2 P_2(\cos\theta) - J_4^{hyd}\left(\frac{r}{r^E}\right)^4 P_4(\cos\theta)\right] \quad (32b)$$

944 where $J_{nhyd} = \bar{\bar{J}}_{nhyd}\left(a_{rE}\right)^n$ (33) 945 Following *Chambat et al. (2010)*, $\bar{J}_2^{hyd}$ is given by the following

first-order accurate expressions:

946 $$\bar{J}_{2hyd} = -\left[f_2(r_E) + m3\right]\left(\frac{a}{a_{hydE}}\right)^2$$

947 ⇒ (using 33) $J_{2hyd} = -[f_2(r_E) + m3](ar_{hyd_E})2$ (34)

948 where $a_{hyd} = r_E[1 - {}^{1}2_{-}$ $f_2(r_E)]$ (35)

949 is the first-order accurate expression for the equatorial radius of the hydrostatic rotating Earth, and

950 $$m = \frac{\Omega 2 r 3}{GM}{}_E \quad (36)$$

951 is the ratio of the centrifugal to mean gravitational acceleration at the mean radius r_E. The degree-2 nondimensional 952 shape coefficient is, to first-order accuracy, given by (*Chambat et al. 2010*):

953 $$f_2(r_E) = -(k_{*fT} + 1)\frac{}{3} m \quad (37)$$

954 where $k^*{}_f{}^T$ is the degree-2 fluid (tidal) Love number. Substituting (35 – 37) into (34) finally yields:

955 $$J_{2hyd} = k_{*fT}\, m\_3\,[1 + (\_\_\_\_\_\_\_\_\_ \_k_{*fT}2 + 1)\, m3\,] \cong k_{*fT}\, m\_3 = k_{*fT}\, \_\_\_\_\_\, \Omega 3\, GM2r_{E3} \quad (38)$$

956 where the last expression in (38) is correct to first-order since $m \ll 1$.

957 Returning to the moment of inertia tensor in (31), the principal polar moment C is identical to the I_{zz} component 958 of the hydrostatic inertia tensor and therefore:

2 Ω 2

959 $C = I_0 + 3\left(\frac{2}{5}\right) Mr_e^2 \left[k_{*fT} \frac{\Omega^2}{3GMr_E^3}\right] = 23\, k_T (*LT_T)\left[(\Omega\Omega_i)^2 - 1\right] Mr_e^2 \left[k_{*fT} \frac{\Omega^2}{3GMr_E^3}\right]$

k_f

960 $\Leftrightarrow$ (using 38) $C = I_0 + \frac{2}{3}(\Omega\Omega_i)^2 Mr_e^2 J_{2hyd} - \frac{2}{T}\left[\left(\frac{\Omega}{\Omega}\right)^2 k_T k(*LT_f)\,\Omega_i^2 - 1\right]$

$Mr_e^2 J_{2hyd}$ (39) 961 Similarly, the two principal equatorial moments $A = B = I_{xx} = I_{yy}$

are then given by:

962 $A = B = I_0 - \frac{1}{3}\left(\frac{\Omega}{\Omega_i}\right)^2 Mr_e^2 J_{2hyd} + \frac{1}{3} k_T k(*LT_{fT})\left[(\Omega\Omega_i)^2 - 1\right] Mr_e^2 J_{2hyd}$ (40)

963 From (38) and (39) we then immediately obtain the following expression for the dynamical flattening of a rotating 964 hydrostatic Earth:

$$H_{hyd} = \frac{C - AC}{I_0 + J_{2hyd} 3\, J_2 Mr_e Mr^2} = \frac{\{e(\Omega\Omega_i)^2 - 2k_T k(LT_{fT}()\underline{LT})\Omega\Omega_i \underline{\Omega^2 i})^2 - 1]\}}{*T}\left[\left(\frac{}{}\right) - 1\right]\Bigg\}$$ (41)

965 H

$\underline{2}_{hyd}{}^2\{(\underline{\Omega\Omega_i}) - \underline{k}\, k_{*fT}\ [(\Omega$

966 In the TPW calculations carried out in this study, we arbitrarily assumed, for simplicity, that $\Omega_i = \Omega$ and in this 967 case (41) simply reduces to:

968 $$H^{hyd} = \frac{J^{hyd} Mr^2}{I_0 + \frac{2}{3} J_2 Mr_e^2}{}_{hyd}{}^2{}_e$$ (42)

From constraints on Earth's mean density structure (*Chambat & Valette 2001*) we have $I_0 = 0.3307 M r_e^2$ and therefore equation (42) yields:

$$H^{hyd} = \frac{J^{hyd}}{0.3307 + 3\,J_2} \qquad (43)$$

To first-order in m, consistent with the accuracy inherent in expression (38), we obtain from (43):

$$\frac{H^{hyd}}{0.3307} \cong \left(\frac{973}{0.3307}\right)\frac{J^2_{hyd}}{\Omega^2}\left(1 - \frac{k^*_f{}^T}{3\,GM}\right) r_E^3 \qquad (44)$$

which reveals the explicit quasi-linear dependence (to first-order accuracy) of the hydrostatic flattening, H^{hyd}, on the square of the rotation rate. Using the following values from *Chambat et al.* (*2010*):

$$m = 3.45016 \times 10^{-3}, \qquad k^*_f{}^T = 0.93233$$

we obtain from the last expression in (38), the following value:

$$J_2{}^{hyd} = 1.0722 \times 10^{-3} \qquad (45)$$

and hence, from (43), we obtain:

$$\boxed{\boldsymbol{H^{hyd}(t=0) = 3.235 \times 10^{-3}}} \qquad (46a)$$

which compares with the following value obtained from (44):

982 $H^{hyd} = 3.242 \times 10^{-3}$ $(46b)$

983 For reference, the value of J_2^{hyd} derived from a second-order accurate solution of the Clairaut

equations is, following *Chambat et al.* (*2010*):

$$J_2^{hyd} = 1.0712 \times 10^{-3} \implies \text{(using 43)} \quad H_{hyd}(t=0) = 3.232 \times 10^{-3} \tag{47}$$

We note that the relative difference between the hydrostatic flattening value in (46a) and (47) is 0.09%, whereas the relative difference between (46b) and (47) is 0.3%, which is of the same order as the convection-induced changes to the dynamic flattening H shown in Figure 4a in the main text. This suggests that expression (43) should be used rather than the less accurate formulation provided in (44). The additional implication is that expression (25) should be used for numerical accuracy when evaluating the additional changes to the time-dependent dynamic flattening H driven by mantle convection.

The largest changes to dynamic flattening $H(t)$ will arise from the deceleration of Earth's rotation rate due to tidal dissipation in the Earth-Moon system. From the many-body orbital solution obtained by *Laskar et al. (2004)* that incorporates luni-solar tidal dissipation, the length of a sidereal day (LOD) 70 million years ago is predicted to be 23.4176 hours, compared to the present-day LOD of 23.9345 hours. The Earth's angular rotation rate at 70 Ma is therefore $\Omega_{70} = 7.453048 \times 10^{-5}$ rad/s (compared to present-day $\Omega_0 = 7.292116 \times 10^{-5}$ rad/s) and, using equations (38) and (43), we obtain

$$J_{hyd}(-70\ \text{Ma}) = \left(\frac{\Omega_{-70}}{\Omega_0}\right)^2 J_{hyd}(0\ \text{Ma}) \Longrightarrow H_{hyd}(-70\ \text{Ma}) = 3.379 \times 10^{-3}$$

$$\Longrightarrow \left[\, \boldsymbol{H^{hyd}(-70\ Ma) - H^{hyd}(0\ Ma)} \,\right] / \boldsymbol{H^{hyd}(0\ Ma) = 45\ ‰} \tag{48}$$

Although the magnitude of this tidal-induced (purely hydrostatic) decrease in Earth's dynamical flattening over the past 70 Ma far exceeds the amplitude of the corresponding convection-induced changes shown in Figure 4a, the perturbation to the precession frequency ω_{prec} (equation 24) arising from mantle convection is nonetheless resolvable in cyclostratigraphic analyses of Eocene-age sediment cores (*Boulila & Hinnov 2022*).

We now consider the signature of the remnant (fossil) rotational bulge in the present-day gravity field and estimate its potential magnitude. For a purely hydrostatic planet, the expression for the polar moment of inertia in equation (39) reduces to:

$$C^{hyd} = I_0 + \frac{2}{3} M r_e^2 J_2^{hyd} \tag{49}$$

A comparison of expressions (39) and (49) reveals the perturbation, denoted by ΔJ_2^{bulge}, to the purely hydrostatic gravitational form factor J_2^{hyd} that arises from the fossil bulge:

$$C = I_0 + \frac{2}{3} \left[\, J_2^{hyd} + \Delta J_2^{bulge} \,\right] M r_e^2 \tag{50}$$

in which

$$\Delta J_2^{bulge} = J_2^{hyd}\ \Delta B(\Omega_i,\ LT), \text{ where } \Delta B(\Omega_i,\ LT) \equiv \left[\ \left(\frac{\Omega}{\Omega_i}\right)^2 - 1 \right] \left[1 - \frac{}{{}^{*T}} k^T k(LT_f) \right] \tag{51}$$

If we arbitrarily assume that the hypothetical fossil bulge was acquired at 250 Ma when, according to the solution of *Laskar et al. (2004)* $\Omega_i = 7.9117 \times 10^{-5}$ rad/s, and again assume that $LT =$ 30 km, we then obtain $\Delta B =$

1015 4.4×10^{-4}. To assess the importance of this value, we consider the value of the nonhydrostatic (or 'dynamic')

1016 value of J_2 defined relative to the satellite-observed value (*Chambat et al. 2010*), $J_2^{obs} = 1.0850 \times 10^{-3}$ (scaled 1017 relative to r_E – see equation 32b) , as follows:

1018 $$\Delta J_2^{dyn} = J_2^{obs} - J_2^{hyd} = J_{2\ hyd} \Delta D, \quad \text{where} \quad \Delta D \equiv \left[\frac{}{J_2} J_{hyd^2 obs} - 1 \right] \quad (52)$$

1019 We thus determine that $\Delta D = 1.3 \times 10^{-2}$, which is two orders of magnitude larger than ΔB, the signal generated

1020 by a fossil bulge, if it formed at 250 Ma. It is therefore not possible to accurately constrain the very small 1021 gravitational signature of a hypothetical fossil bulge using the present-day nonhydrostatic degree-2 geoid. 1022 Finally, we may use the value of J_2^{obs}, and the extension of expression (42) to a dynamic (nonhydrostatic) Earth, 1023 to determine the 'observed' present-day dynamical flattening (see also Table 6 in *Chambat & Valette 2001*):

1024 $$H^{obs} = \frac{}{0.3307 + \frac{2}{3} J_2^{obs}} J^{2obs} \quad \Rightarrow \quad \boxed{H^{obs}(t = 0) = 3.2738 \times 10^{-3}} \quad (53)$$

1025

1026 **8. Impact of Tidal Deceleration on TPW**

1027 As discussed in detail in the preceding section, secular changes in Earth's rotation rate due to tidal dissipation will

1028 alter the hydrostatic contributions to the moment of inertia tensor, via the J_2^{hyd}coefficient, that vary with the square 1029 of the rotation rate (see equations 38 to 40). These long-term, rotation-induced variations in the moments of inertia

should therefore have some impact on TPW (*Greff-Lefftz 2011*). We may assess the magnitude of this impact by

first noting that the time derivative of Earth's angular rotation vector, $\boldsymbol{\omega}(t)$, may be decomposed as follows:

$$\dot{\boldsymbol{\omega}} = \frac{d\hat{\boldsymbol{\omega}}\,\Omega}{dt} = \hat{\boldsymbol{\omega}}\,\Omega + \hat{\boldsymbol{\omega}}\,\dot{\Omega} = \Omega\left[\hat{\boldsymbol{\omega}} + \hat{\boldsymbol{\omega}}\frac{\dot{\Omega}}{\Omega}\right] \tag{54}$$

where $\hat{\boldsymbol{\omega}}(t) \cdot \hat{\boldsymbol{\omega}}(t) = 1$ and $\Omega(t) = \|\boldsymbol{\omega}(t)\|$ is the rotation speed. This expression allows us to directly distinguish the relative magnitude of TPW rates, the first term in brackets in (54), compared to the secular rate of decrease of rotation rate, the second term in brackets. The decomposition (54) also makes clear that the changes in the rotation vector $\boldsymbol{\omega}(t)$ due to TPW are always orthogonal to the changes in the rotation vector due to tidal deceleration, because $\hat{\boldsymbol{\omega}} \cdot \dot{\hat{\boldsymbol{\omega}}} = 0$. Figure 3 in the main text shows that the average magnitude of convection-induced TPW rates over the past 70 Ma is about: $\|\dot{\hat{\boldsymbol{\omega}}}\| = 0.2°/\text{Ma} = 3.5 \times 10^{-3}\ \text{Ma}^{-1}$. The *Laskar et al.* (*2004*) orbital solution yields the present-day value $\dot{\Omega}/\Omega = -9.8 \times 10^{-18}\text{s}^{-1} = -3.1 \times 10^{-4}\ \text{Ma}^{-1}$. We thus find that the relative impact of tidal deceleration on the secular evolution of Earth's 'wandering' rotation vector is: $\|\dot{\hat{\boldsymbol{\omega}}}\,\Omega\| / \|\dot{\hat{\boldsymbol{\omega}}}\,\dot{\Omega}\| \approx 9\%$.

We can further assess the effect of tidal deceleration on convection-induced TPW by substituting expression (54) into equation (18), which then yields the following revision to equation (19):

$$-\left[\frac{3 r_e G_5 k_{fT}}{(LT)\,\Omega^2(t)\,T_1}\right]\Omega(t)\,\hat{\boldsymbol{\omega}}(t) + \Omega(t)\,\underline{\boldsymbol{\delta I}^S}(t)\cdot\hat{\boldsymbol{\omega}}(t) = \lambda\,\Omega(t)\hat{\boldsymbol{\omega}}(t)$$

$$\Leftrightarrow \quad -\left(\frac{\dot{\Omega}}{\Omega(t)}\right)\left[\frac{3 r_e G_5 k_{fT}}{(LT)\,\Omega_0\,T_1}\right]\hat{\boldsymbol{\omega}}(t) + \underline{\boldsymbol{\delta I}^S}(t)\cdot\hat{\boldsymbol{\omega}}(t) = \lambda\,\hat{\boldsymbol{\omega}}(t) \tag{55}$$

where $\Omega_0 = \Omega(0)$ is the present-day rotation speed. From equation (55) we again obtain equation (20) because $\boldsymbol{\omega\hat{}} \cdot \boldsymbol{\omega\hat{}} = 0$, finally yielding the following revision of equation (23):

$$\beta\, T_1\, \boldsymbol{\omega\hat{}}(t) = \left(\frac{\Omega_0}{\Omega(t)}\right)^2 \left[\underline{\boldsymbol{\delta I}^S}(t) - \left\{\hat{\boldsymbol{\omega}}(t) \cdot \underline{\boldsymbol{\delta I}^S}(t) \cdot \hat{\boldsymbol{\omega}}(t)\right\} \underline{\boldsymbol{I}}\right] \cdot \hat{\boldsymbol{\omega}}(t) \quad (56)$$

in which β is again defined as in expression (23b):

$$\beta = \frac{3 e G\, k_f^T(LT)}{r_5\, \Omega_0^2} \quad (57)$$

From (56) we thus see that the secular decrease in Earth's rotation speed will essentially modulate the amplitude of TPW velocity and minimally alter the geometric shape of the TPW trajectory. This expression also shows there is a damping of TPW that grows with the inverse-squared of the rotation speed due to the larger rotational bulge. Based on the solution in *Laskar et al.* (*2004*), the secular decrease in rotation speed due to tidal braking over the past 100 Ma is about 3% and hence the rotational damping of the TPW speed, on the right-hand side of (57), will decrease by about 6%. We note that these small effects on TPW from tidal deceleration (at least over the time span studied here) are supported by the earlier investigation by *Greff-Lefftz* (*2011*).

From the preceding considerations, we then write the following approximate expression that may be employed to incorporate the influence of tidal deceleration on the rate of change of Earth's rotation vector:

$$\dot{\boldsymbol{\omega}} = \frac{d\boldsymbol{\omega\hat{}}\,\Omega}{dt} = \dot{\boldsymbol{\omega\hat{}}}\,\Omega + \boldsymbol{\omega\hat{}}\,\dot{\Omega} \approx \dot{\Omega}(t)\, \hat{\boldsymbol{\omega}}(t) \quad (58)$$

We may now revise expression (12), representing the time-dependent moment of inertia tensor, to also include secular changes in the rotation rate, via equation (54), as follows:

$$I_{i,j}(t) = I_0\,\delta_{i,j} + \frac{r^5}{{}^{e}}\,\Omega 3G^2(t)\,k_f{}^T(LT)\{[\hat{\omega}_i\hat{\omega}_j - \overline{3}\,\delta_{i,j}] - T_1\,[(\hat{\omega}_{\,i} + \hat{\omega}_i\,\Omega\,\Omega\,)\,\hat{\omega}_j + \hat{\omega}_i\,(\hat{\omega}_j + \hat{\omega_j}\,\Omega\Omega\,\overline{3}\,) - \Omega\Omega\,\delta_{i,j}]\,\}$$

$$+\,3\,\frac{r_5}{}\,\left[\,k^{*T}_f - k^T_f(LT)\,\right]\,{}^{2}\,\frac{1}{}\,3\,{}^{e}G\qquad \Omega_i\,(\delta_{i,3} - \_)\,\delta_{i,j} + \delta I_{i,j\mathrm{con}}(t)$$

Using approximation (58), the preceding expression finally simplifies to:

$$I_{i,j}(t) = I_0\,\delta_{i,j} + M_E r_e{}^{2}\,\frac{\overset{\frown}{\mathrm{J}_{hyd}}}{3\;\;2}\,\frac{{}_{2}\;(0)}{0}\,\Omega_0\,\frac{r\,\Omega}{}\,{}^{*}_{f}\,\left[k^{*T}\,\frac{}{}\right]\left\{\left(\frac{}{}\right)^{2}\,\frac{k^T(LT)}{3}\,\frac{1}{}\,\left(\frac{\Omega}{\Omega}\,\frac{k^T_f(LT)^2}{k_{fT}}\,\frac{1}{}\,[\hat{\omega}_i\hat{\omega}_j - \_\,\delta_{i,j}] - T_1[\hat{\omega}_{\,i}\hat{\omega}_j + \hat{\omega}_i\hat{\omega}_j]\right)\right.$$

$$\left. +\left(\frac{i}{}\right)\,\left[\,1 - \frac{}{T}\,\right]\,(\delta_{i,3} - \_)\,\delta_{i,j}\right\} + \delta I_{i,j}{}^{\mathrm{con}}(t) \qquad (59)$$

$$\Omega_0\qquad k^*_f\qquad 3$$

This representation for Earth's moment of inertia tensor will be employed in our modelling of the time-dependence of dynamic flattening, $H(t)$ in equation (25), that includes the effects of tidal deceleration and of mantle convection-induced changes to the inertia tensor via the direct contribution $\delta I_{i,j}{}^{\mathrm{con}}(t)$ and also via the contribution to the horizontal displacements (i.e. TPW) of Earth's rotation vector $\boldsymbol{\hat{\omega}}$(t). In all cases, we determine the principal moments needed to predict the value for $H(t)$ via a numerical calculation of the eigenvalues of the inertia tensor.

9. Modelling Earth-Moon Separation via Angular Momentum Conservation

Tidal dissipation in the Earth–Moon system not only generates a secular decrease of Earth's rotation speed, discussed above, it will also induce a so-called "recession" of the Moon, as the Earth-Moon distance increases.

Both effects, namely secular changes in rotation speed $\Omega(t)$ and Earth-Moon separation $a_L(t)$, will strongly impact the time evolution of Earth's astronomical precession frequency $\omega_{prec}(t)$, described in equation (24), which arises from the luni-solar torques acting on Earth's rotational bulge represented by the dynamical flattening $H(t)$. The impact of the secular decrease in rotation speed over the past 70 Ma, as noted above in expression (48), will be large. To also quantify the impact of secular changes in Earth-Moon separation $a_L(t)$ on precession, we use angular momentum conservation, as in *Lambeck* (*1977*), *Schwiderski* (*1985*) and most recently in *Farhat et al.* (*2022b*), which has long been the basis (*Darwin 1908*) for modelling the connection between tidally driven changes of Earth's rotation speed and variable Earth-Moon distance.

More recently, *Tian & Wisdom* (*2020*) presented numerical and theoretical demonstrations that the vertical component of the total angular momentum vector of the Earth-Moon system, L_z – defined relative to the ecliptic plane, is effectively conserved (to one part in a thousand) as the Earth-Moon separation evolves from $5r_E$ to $50r_E$, where r_E is the mean radius of the Earth. As noted by the authors, this quasi-conservation obtains in the absence of any resonances. Therefore, following *Lambeck* (*1977*) and *Tian & Wisdom* (*2020*), we employed the following simplified representation of the vertical component of the total Earth-Moon angular momentum:

$$L^{total}{}_z = C_E\,\Omega\cos\varepsilon + m_L\sqrt{GM_E\,a_L\,(1-e_L^2)}\cos i_L \qquad (60)$$

where the first term on the right-hand side is the spin angular momentum of the Earth, in which C_E is the polar moment of inertia of the Earth, Ω is the diurnal rotation rate and ε is the obliquity angle, whereas the second term is the Moon's orbital angular momentum in which m_L and M_E are the mass of the Moon and Earth, respectively,

a_L is the semi-major axis of the lunar orbit, e_L is the eccentricity of the lunar orbit and i_L is the inclination of the orbit relative to the ecliptic (see Table S1). The second term has been derived appealing to Kepler's Third Law for the mean motion of the Moon. In (60) we ignored the spin momentum of the Moon and the orbital momentum of the Earth relative to the barycentre of the Earth-Moon system since both are negligibly small relative to the spin momentum of the Earth and orbital momentum of the Moon, respectively.

If the application of angular momentum conservation in (60) were extended to encompass the Sun-Earth-Moon system, the vertical component of the orbital angular momentum of the Earth around the Sun, $L^{Sun}{}_z$, would completely dominate, being many orders of magnitude larger than any contribution within the Earth-Moon system. However, as underlined by *Lambeck* (*1977*), angular momentum transfer between Earth and Sun is infinitesimally small and Earth's orbit has therefore undergone negligible solar-tidal evolution. $L^{Sun}{}_z$ may thus be treated as a constant. But dissipation from solar tides on the Earth is not negligible and will contribute to a secular reduction of Earth's spin momentum and rotational kinetic energy (*Lambeck 1977*), without altering the Earth's continuous transfer of angular momentum to the Moon's orbit via the torque exerted by Earth's tidal bulge on the Moon. This contribution from the Sun will be explicitly quantified in the considerations presented below.

From the many-body orbital solution provided by *Laskar et al.* (*2004*), henceforth denoted as "La2004", we employed their predictions for the time-dependent rotation rate $\Omega(t)$ and semi-major axis $a_L(t)$, while holding the obliquity ε, eccentricity e_L, and inclination i_L fixed at their present-day values, to determine the evolution of $L^{total}{}_z$

over the past 70 million years. In this calculation, we model the variation of Earth's polar moment of inertia C_E with changing Ω, according to equations (38) and (39), as follows:

$$C_E(t) = C_E(0) + \frac{2}{3}\frac{k^*{}_f{}^T r^5}{3\,G}[\Omega^2(t) - \Omega^2{}_0] \qquad (61)$$

The predicted $L^{total}{}_z$ shown in Figure S4(a) varies from a present-day value of $3.3942 \times 10^{34}\ kg\ m^2 s^{-1}$ to a

value at 70 Ma of $3.3958 \times 10^{34}\ kg\ m^2 s^{-1}$, representing a small change of 0.5‰ that is well within the tolerance described by *Tian & Wisdom (2020)*.

We now examine this result more critically and explore whether the very slight, linear decrease of $L^{total}{}_z$ evident in Figure S4(a) may rectified, such that $L^{total}{}_z$ remains constant (or nearly so) over the past 70 Ma. We begin by noting that Earth-Moon angular momentum conservation, as described in expression (60), has traditionally been employed (e.g. *Lambeck 1977*) to model the rate of recession of the Moon: $\dot{a}_L \equiv da_L/dt$. The time-derivative of (60) yields:

$$\dot{a}^L = -\left(\frac{2\,C_E \cos\varepsilon \sqrt{a_L}}{m_L \sqrt{GM_E}(1-e_L^2)\cos i^L}\right)\Omega \qquad (62)$$

in which we treated C_E, ε, i_L, and e_L as effectively constant and $\Omega \equiv d\Omega/dt$. This approximation is maintained throughout the work that follows. Using the La2004 values for Ω and $\dot{a}_L$ over the past 70 Ma, we find that they cannot be reconciled by equation (62). The La2004 prediction for the secular rate of change of Earth's rotation rate, Ω, when substituted into (62), yields a predicted recession rate $\dot{a}_L$ that is systematically larger than the recession rate output by La2004. The La2004 lunar recession rate can only be fit, in the context of equation (62), by reducing the La2004 secular deceleration Ω by a (nearly constant) factor of 0.85 ± 0.01 throughout the past 70 Ma.

This apparently ad-hoc reconciliation can be justified by recognizing that the total tidal dissipation of energy in the Earth-Moon system also includes the dissipation of solar tides raised on the Earth and therefore the secular deceleration of Earth's rotation rate, Ω, contains two distinct contributions (*Lambeck 1977*) : (1) a deceleration

1133 denoted by Ω_L arising from lunar tidal dissipation and (2) a deceleration denoted by Ω_S arising from solar tidal 1134 dissipation, which does not contribute to the Earth-Moon momentum balance in expression (60). We thus write:

1135 $$\Omega = \Omega_L + \Omega_S, \text{ where } \frac{\dot{\Omega} L}{\Omega} \equiv \alpha_L \cong 0.85 \pm 0.01 \Longrightarrow \frac{\dot{\Omega} \dot{S}}{\Omega} \equiv \alpha_S \cong 0.15 \pm 0.01 \quad (63)$$

1136 When the value of Ω_L given by (63) is employed instead of Ω in expression (62), we obtain a very good match to 1137 the lunar recession rate $\dot{a}_L$ predicted by La2004 over the past 70 Ma.

1138 We briefly consider the implications of the luni-solar partitioning of Earth's secular deceleration, in (63), for the 1139 rate of energy dissipation in the Earth-Moon system. The power of lunar and solar dissipation of energy, denoted

1140 respectively by P_L and P_S, is determined by the corresponding dissipative tidal torques, denoted by $\mathcal{T}_L$ and $\mathcal{T}_S$, such

1141 that:

1142 $P_L = \mathcal{T}_L \Omega$ and $P_S = \mathcal{T}_S \Omega$, where $\mathcal{T}_L = C_E \Omega_L$ and $\mathcal{T}_S = C_E \Omega_S \Longrightarrow P_L = C_E \Omega_L \Omega$ and $P_S = C_E \Omega_S \Omega$

1143 $$\Longrightarrow \quad P_{\text{Total}} = P_L + P_S = C_E (\Omega_L + \Omega_S) \Omega = C_E \Omega \dot{\Omega} = \frac{dE_{rot}}{dt}, \text{ where } E_{rot} = \frac{1}{2} C_E \Omega^2 \quad (64)$$

1144 where dE_{rot}/dt is the rate of change of Earth's rotational energy. Employing present-day values for rotation rate

1145 Ω and secular deceleration $\dot{\Omega}$ from La2004, and the present-day value for Earth's polar moment of inertia C_E, the 1146 rate of dissipation of rotational energy, as defined in (64), is $dE_{rot}/dt = 4.2\ TW$ of which 85% (i.e. $3.6\ TW$) is 1147 due to lunar tidal dissipation. These dissipation values are of course an expression of the tidal dissipation model

1148 assumed in La2004 and are comparable to independent estimates of tidal dissipation obtained by *Egbert and Ray* 1149 (*2003*) who find present-day total dissipation is ~3.5 TW, of which ~0.5 TW is due to solar tides and hence the 1150 latter contribute about 14% of the total dissipation. Expression (64) for tidal energy dissipation manifested in the

decrease of Earth's rotational kinetic energy does not include the small (~3%) rate of increase of energy transferred to the lunar orbit as result of the recession of the Moon (*Lambeck 1977*). (The inclusion of the latter contribution leads to the mathematical representation for total energy dissipation by lunar tides developed in *Murray & Dermott 1999*).

Based on expression (63), we obtain the following linearized approximation to the time-dependent rotation rate, in which we isolate the contribution due only to the deceleration arising from lunar tidal dissipation:

$$\Omega(t) = \Omega_0 + \dot{\Omega}_0 t = \Omega_0 + \alpha_L \dot{\Omega}_0 t + (1 - \alpha_L)\dot{\Omega}_0 t$$

$$\Leftrightarrow \Omega(t) = \underbrace{\Omega_0 + \Delta\Omega_L(t)}_{\equiv \Omega_L(t)} + \Delta\Omega_S(t), \text{ where } \Delta\Omega_L(t) = \alpha_L \dot{\Omega}_0 t \text{ and } \Delta\Omega_S(t) = (1 - \alpha_L)\dot{\Omega}_0 t \quad (65)$$

where $\Omega_L(t)$ represents the (dominant) lunar-tidal contribution to the time-varying rotation rate of the Earth. We return to expression (60), in which $\Omega(t)$ is now replaced by $\Omega_L(t)$ and we thus obtain:

$$L^{total}_z = C_E(t)\Omega_L(t)\cos\varepsilon + m_L\sqrt{GM_E\, a_L(t)(1 - e_L^2)}\cos i_L \quad (66)$$

where we again use the rotation-rate dependence of the polar moment of inertia given in (61). Using the values for $a_L(t)$ and $\dot{\Omega}_0$ from La2004, using $\alpha_L = 0.85$ (see 65) and other parameters from Table S1, we recalculate L^{total}_z and now find (see red curve in Figure S4(a)) that L^{total}_z varies at most by 0.03‰ over the past 70 Ma, confirming the near-constancy of the total angular momentum.

With this last result in hand, we can now derive a simple, closed-form expression for the time-dependence of the semi-major axis of the lunar orbit, $a_L(t)$, using the revised expression for angular momentum conservation in (66), thus yielding:

$$a_L(t) = \frac{[L_{total} - C_E(t)\left(\Omega_0 + \alpha_L\dot{\Omega}_{z,0}t\right)\cos\varepsilon]^2}{(m_L\cos i_L)^2\, GM_E\,(1 - e^2)_L} \quad (67)$$

in which $L^{total}_{z,0}$ is the total, Earth-Moon angular momentum calculated with present-day values for the variables

appearing in (60) and $C_E(t)$ is calculated, according to equation (61), assuming that $\Omega(t) = \Omega_0 + \Omega_0 t$. We again assume that ε, i_L, and e_L remain constant. In Figure S4(b) (see red curve) we verify expression (67) against the time-evolution of $a_L(t)$ provided by the La2004and find an excellent match over the past 70 Ma. The largest deviation relative to the La2004 values for $a_L(t)$, obtained at 70 Ma, is only 0.06‰. (This close match is perhaps better than one should expect, given our assumption of constant ε, i_L, and $e_L$over the past 70 Ma!)

The closed-form expression (67) provides a useful tool for exploring the impact of changing luni-solar tidal dissipation rates over the past 70 Ma, by simply adjusting the value of Ω_0. This adjustment will directly translate into corresponding adjustments in the tidal-dissipation power, as shown in (64). We explored two scenarios: (1) The first scenario is motivated by the modelling of *Green et al.* (*2017*), who estimated changes in tidal dissipation over the past 252 Ma using paleogeographic reconstructions and found that tidal dissipation was much weaker than at present over a long interval of time preceding the Pliocene. These authors infer past rates of tidal dissipation that were 50% lower than present-day rates, and perhaps as low as 30% of present-day during the Paleocene Eocene. They therefore proposed that the modern, high rates of tidal dissipation are distinctly anomalous relative to the reconstructed pre-Pliocene rates. (2) The second scenario is a hypothetical case study in which we assume that tidal dissipation was reduced to 30% of the present-day value for times earlier than 35 Ma. This time corresponds to the beginning of permanent glaciation over Antarctica and the corresponding drop in global mean sea level by about 58 metres (corresponding to the current ice mass in Antarctica). It is thus hypothesized that the resulting shallowing of global bathymetry, and the development of the Antarctic Circumpolar Current after the opening of the Drake Passage and Tasman Gateway, led to greater rates of tidal dissipation over the past 35 Ma, compared to pre-Oligocene rates. This admittedly speculative scenario is explored to investigate the degree to which the precession frequency will be perturbed by large changes in tidal dissipation, at earlier times in the past (relative to scenario 1). Both scenarios are motivated by the paleo-tidal modelling simulations by *Green et al.* (*2017*) and their implications for the history of Earth-Moon separation (calculated with equation 67) are presented

in Figure S4(b), where we used (67) with changes to Ω_0 at 5 Ma, or 35Ma, and we found that both scenarios lead to between 1000 and 1300 km less lunar recession than predicted by the La2004 model.

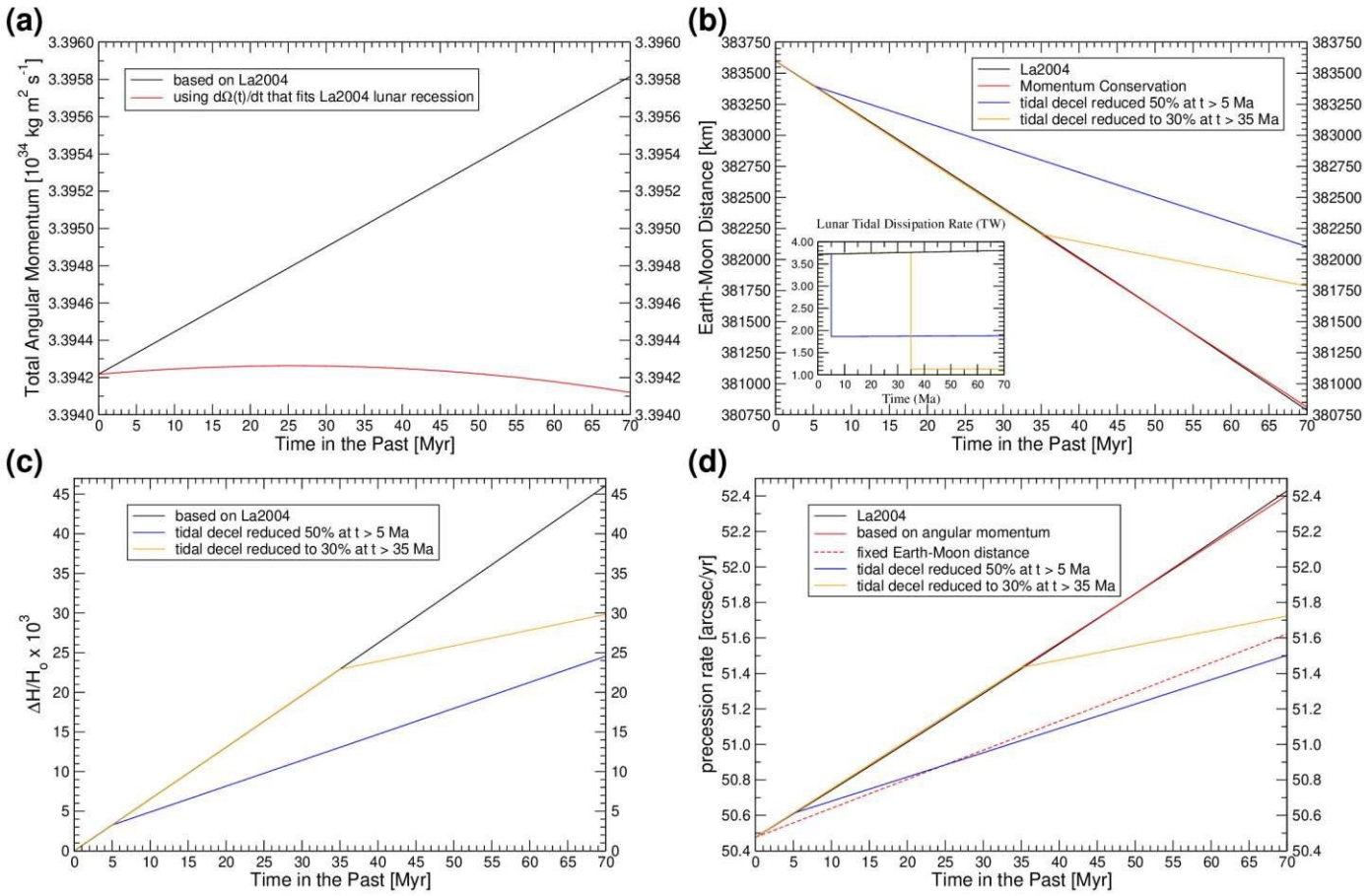

Figure S4: **Modelling changes of Earth's precession rate due to secular deceleration of Earth rotation and Earth-Moon separation. (a)** Modeled total angular momentum of the Earth over the past 70 million years, based on equation (60). The black curve represents predictions based on the variations of rotation-rate and Earth-Moon distance given by the La2004 model. The red curve shows the total angular momentum calculated only including rotation-rate changes due to lunar tidal deceleration: see equation (66). **(b)** Changes in the Earth-Moon distance over time. The black curve shows the prediction from the La2004 model, while the red curve represents the EarthMoon distance calculated using equation (67), derived from angular momentum conservation. The blue curve illustrates a scenario with tidal deceleration reduced to 50% of the present-day value for times greater than 5 million years ago, and the orange curve depicts a scenario where tidal deceleration is reduced to 30% of present day for times greater than 35 million years ago. The inset graph shows the corresponding lunar tidal dissipation rates (in TW), demonstrating the energetic implications of different tidal deceleration scenarios. **(c)** Changes in Earth's dynamic flattening, $\Delta H(t)/H_0$, defined in equation (30) and modelled using equation (69). The black curve is the prediction obtained using the time dependence of rotation rate in equation (65) and using the present-day deceleration, Ω_0, from La2004. The blue curve represents the prediction assuming reduced tidal deceleration (50%) for times greater than 5 million years ago, and the orange curve shows changes with tidal deceleration reduced to 30% for times greater than 35 million years ago. These results underscore the significant variability in dynamic flattening due to tidal dissipation. **(d)** Modeled precession rate of the Earth over the past 70 million years. The black curve corresponds to La2004 model predictions. The red solid curve represents a prediction based on equation (71), using a_L calculated from angular momentum conservation (equation 67) and the present-day rate of

deceleration, Ω_0, from La2004, used in equation (65). The red dashed curve is the corresponding prediction holding the Earth-Moon distance a_L fixed to present-day value. The blue curve reflects the predicted precession rate with 50% reduced tidal deceleration for times greater than 5 million years ago, and the orange curve depicts the precession rate with tidal deceleration reduced to 30% for times greater than 35 million years ago.

10. Secular Influence of Variable Tidal Dissipation on Dynamic Flattening and Precession

As discussed above (in section 9), we explored two scenarios where tidal dissipation is reduced at $t = -5$ Ma or -35 Ma, to explore the impact on the evolution of Earth-Moon distance $a_L(t)$, compared to the La2004 solution (Figure S4(b)). We now consider the implications for Earth's dynamical flattening $H(t)$, defined in (25), and for precession frequency $\omega_{prec}(t)$, defined in (24).

The present-day ('observed') value of dynamic flattening, given by the IERS (*International Earth Rotation and Reference Systems*) Conventions of 2010 (*Petit & Luzum 2010*) is:

$$H^{obs}(0) = 3.273795 \times 10^{-3} \qquad (68)$$

This value compares with the present-day hydrostatic value (see equations 46, 47): $H^{hyd}(t=0) = 3.235(\pm 5) \times 10^{-3}$, where the uncertainty in the last significant figure stems from the (1st or 2nd order) accuracy employed in the determination of $J_2^{hyd}(0)$.

If we assume that Earth's angular rotation vector is $\boldsymbol{\omega}(t) = \Omega(t)\,\hat{\boldsymbol{z}}$, which implies that we ignore TPW, and we follow the derivations that led to equation (43), but also include a contribution from internal dynamics – defined in equation (52), we then obtain the following expression for Earth's time-dependent dynamic flattening:

$$H(t) = \frac{J_2^{hyd}(0)\,\frac{\Omega^2(t)}{\Omega_2} + \Delta J_2^{dyn}(t)}{0.3307 + 3\,[J_2^{hyd}(0)\,\frac{\Omega_0^2}{\Omega_2} + \Delta J_2^{dyn}(t)]} \qquad (69)$$

in which we used the rotation-rate dependence of J_2^{hyd} given in equation (38), $J_2^{hyd}(0)$ is the present-day value

given and $\Delta J_2^{dyn}(t)$ represents the time-dependent contribution to Earth's flattening from dynamical (nonhydrostatic) processes, notably mantle convection and glacial isostatic adjustment. For the secular variation of the rotation rate, we again assume the following linearized expression from (65): $\Omega(t) = \Omega_0 + \dot{\Omega}_0 t$, where we can adjust $\dot{\Omega}_0$ at different times in the past, as in the two scenarios that explored (see section 9) the impact of reduced tidal dissipation in the past. We also constrain $\Delta J_2^{dyn}(t = 0)$ such that expression (69) exactly yields the same value for $H(0)$ as $H_{obs}(0)$ in (68), and for this purpose we also used $J_2^{hyd}(0)$ from equation (47). We then kept ΔJ_2^{dyn} fixed to its present-day value to show the temporal variations of $H(t)$ that would result only from tidal deceleration. In our first simulation, we modelled the secular decrease of rotation rate using $\dot{\Omega}_0$ from La2004 and the resulting variation of $H(t)$ over the past 70 Ma is shown in Figure S4(c). The 46‰ change over this time interval far exceeds any changes to $H(t)$ that may be predicted by mantle convection (see Figure 4 in the main text). We also considered the two scenarios described in section 9, in which tidal dissipation (TD) is strongly reduced relative to present-day: (1) prior to 5 Ma, TD is reduced to 0.5 of present-day, and (2) prior to 35 Ma, TD is reduced to 0.3 of present-day. The resulting impact of such reductions in TD on the evolution of $H(t)$ is large, as shown in Figure S4(c), and they greatly exceed any changes that would likely be driven by mantle convection (Figure 4).

In previous modelling of secular changes in $H(t)$ and their influence on Earth's precession frequency $\omega_{prec}(t)$, via equation (24), *Farhat et al.* (*2022b*) employed a value $H(0) = 3.243 \times 10^{-3}$, which is essentially that predicted (to 1st-order accurate theory) for a purely hydrostatic planet (see equations 44 and 46b), and they model its variation with rotation as follows: $H(t) = H(0) \times \Omega^2(t)/\Omega^2_0$ (compare with equation 69). Similarly, *Boulila & Hinnov* (*2022*) also model precession with equation (24), assuming a hydrostatic flattening, $H(0) = 3.24 \times 10^{-3}$, assuming an Ω^2 dependence as in *Farhat et al.* (*2022b*). We examine the implications of these flattening values for the predicted present-day precession frequency $\omega_{prec}(0)$, using equation (24). The additional

1235 inputs required for equation (24) are listed in Table S1. With these tabulated parameters and the different values

1236 for present-day dynamical flattening discussed above, equation (24) yields the following predictions:

$$\omega_{prec}(0) = \begin{cases} 50.7223\ "/\text{yr} \ \text{ for } \ H^{obs} = 3.273795 \times 10^{-3} \ \ (eq.\ 68) \\ 50.0747\ "/\text{yr} \ \text{ for } \ H^{hyd} = 3.232 \times 10^{-3} \qquad (eq.\ 47) \\ 50.1212\ "/\text{yr} \ \text{ for } \ H^{hyd} = 3.235 \times 10^{-3} \qquad (eq.\ 46a) \end{cases} \tag{70}$$

1237

1238 compared to (from La2004): $\omega_{prec}{}^{La2004}(0) = 50.4758\ "/\text{yr}$

1239 All three predictions in (70) differ from the present-day precession frequency in the La2004 solution $\omega_{prec}{}^{La2004}(0)$.

1240 While calculating the results in (70), it became apparent that the predicted precession values are quite sensitive to

1241 small changes of the input parameters in Table S1, notably a_L and ε. The magnitude of the differences in (70) 1242 relative to La2004 can be regarded as large in the context of cylcostratigraphy and they would be detectable in

1243 these analyses (*Pälike & Shackleton 2000*).

1244 In a further effort to examine whether the present-day flattening in (68) may be reconciled with the value of

1245 $\omega_{prec}{}^{La2004}(0)$, we next considered a somewhat more refined theoretical expression for the precession frequency that 1246 is taken from equations (6) and (8) in La2004:

$$\omega_{prec} = \frac{3}{2}\frac{H}{\Omega}\left[\frac{GM_S}{\left(a_S\sqrt{1-e_S{}^2}\right)^3} + \frac{Gm_L}{\left(a_L\sqrt{1-e_L{}^2}\right)^3}\left(1 - \frac{3}{2}\sin^2 i_L\right)\right]\cos\varepsilon \tag{71}$$

1247

1248 The additional input parameters appearing in (71) are defined in Table S1. We again repeated the calculations for

1249 ω_{prec}, using expression (71), and obtained the following results:

$$\omega_{prec}(0) = \begin{cases} 50.4655\ "/\text{yr} \ \text{ for } \ H^{obs} = 3.273795 \times 10^{-3} \ \ (eq.\ 68) \\ 49.8212\ "/\text{yr} \ \text{ for } \ H^{hyd} = 3.232 \times 10^{-3} \qquad (eq.\ 47) \\ 49.8675\ "/\text{yr} \ \text{ for } \ H^{hyd} = 3.235 \times 10^{-3} \qquad (eq.\ 46a) \end{cases} \tag{72}$$

1250

1251 compared to (from La2004): $\omega_{prec}{}^{La2004}(0) = 50.4758\ "/\text{yr}$

We now can very nearly reconcile the value of H^{obs} with the present-day precession frequency predicted by the orbital solution of La2004. The difference between the two precession values is only 0.2‰. We therefore employed expression (71) for all predictions of the precession frequencies that are presented in the main text (Figure 4) and in the following discussion.

The key time-dependent variable that appears in (71), apart from the dynamic flattening $H(t)$ (see Figure S4(c)), is the Earth-Moon semi-major axis: $a_L(t)$. We performed a first simulation in which we modelled Earth-Moon separation according to (67), and $H(t)$ according to (69) – again keeping $\Delta J_2{}^{dyn}$ fixed to its present-day value, and using the present-day deceleration rate from La2004. We obtained very good agreement with the time-dependent $\omega_{prec}{}^{La2004}(t)$ values from La2004 over the past 70 Ma, as shown by the black and red curves in Figure S4(d). The average difference between the two curves over the entire 70 Ma interval was 0.4‰. In a sensitivity experiment, we ran another simulation keeping the Earth-Moon separation fixed to present-day value while allowing the $H(t)$ to evolve as before, and the result (see dashed red curve in Figure S4(d)) shows that the variation in $H(t)$ alone contributes 55% of the total change in $\omega_{prec}{}^{La2004}(t)$ over the past 70 Ma, with the other 45% due to the change in Earth-Moon separation. Finally, we calculated the evolution of $\omega_{prec}(t)$ for the two scenarios in which TD was 0.5 of present-day prior to 5 Ma, and TD was 0.3 of present-day prior to 35 Ma. The results, shown by the blue and orange curves in Figure. S4(d), reveal that these hypothetical changes in TD have a large impact that should be detectable in cyclostratigraphic analysis of pre-Pliocene age sedimentary sequences, especially in the Paleogene period.

Table S1: Values of input parameters for the numerical calculation of angular momentum and precession rate

Solar gravitational constant: GM_S (*IAU 2009*)	1.3271244×10^{20} m^3s^{-2}
Earth's gravitational constant: GM_E (*IAU 2009*)	3.9860044×10^{14} m^3s^{-2}

Lunar gravitational constant: Gm_L (From *IAU 2009* value for $m_L/M_E = 1.23000371 \times 10^{-2}$)	4.902800×10^{12} m^3s^{-2}
Constant of gravitation: G (*IAU 2009*)	6.67428×10^{-11} $m^3kg^{-1}s^{-2}$
Earth orbit semi-major axis: a_S (*IAU 2009*)	1 au = $1.495978707 \times 10^{11}$m
Lunar orbit semi-major axis: a_L (From *JPL DE440/DE441 Ephemerides*)	384399×10^3m
Present-day sidereal rotation rate: Ω_0 (*IAU 2009*)	7.292115×10^{-5} s^{-1}
Present-day obliquity of the ecliptic: ε (From $t = 0$ orbital solution of *Laskar et al. 2004*)	23.270773°
Present-day lunar inclination to the ecliptic: i_L (from *Williams & Boggs 2016*)	5.145°
Present-day eccentricity of Earth orbit: e_S (from *Simon et al. 1994*)	0.0167086
Present-day eccentricity of lunar orbit: e_L (from *Williams & Boggs 2016*)	0.0549

References (Supplementary Information):

Chambat, F., & Valette, B. (2001). Mean radius, mass, and inertia for reference Earth models. *Physics of the Earth and Planetary Interiors*, 124(3-4), 237-253.

Chan, N. H., Mitrovica, J. X., Daradich, A., Creveling, J. R., Matsuyama, I., & Stanley, S. (2014). Time-dependent rotational stability of dynamic planets with elastic lithospheres. *Journal of Geophysical Research: Planets*, 119(1), 169-188.

Darwin, G.H. (1908). The Scientific Papers of Sir George Darwin: "*Tidal Friction and Cosmogony*". *Volume 2*. Cambridge University Press.

Egbert, G. D., & Ray, R. D. (2003). Semi-diurnal and diurnal tidal dissipation from TOPEX/Poseidon altimetry. *Geophysical Research Letters*, 30(17).

Farhat, M., Auclair-Desrotour, P., Boué, G., & Laskar, J. (2022b). The resonant tidal evolution of the Earth-Moon distance. *Astronomy & Astrophysics*, 665, L1.

Forte, A. M., & Peltier, W. R. (1987). Plate tectonics and aspherical Earth structure: The importance of poloidaltoroidal coupling. *Journal of Geophysical Research: Solid Earth*, 92(B5), 3645-3679.

Goldstein, Herbert (1980). *Classical Mechanics*. Second Edition. Addision-Wesley.

Lambeck, Kurt (1977). Tidal dissipation in the oceans: astronomical, geophysical and oceanographic consequences. *Philosophical Transactions of the Royal Society of London*. Series A, Mathematical and Physical Sciences, 287(1347), 545-594.

Murray, C. D., & Dermott, S. F. (1999). "*Solar System Dynamics*". Cambridge University Press.

Petit, G., & Luzum, B. (2010). IERS conventions. *IERS technical note*, 36(1), 2010.

Press, W. H., Teukolsky, S. A., & Vetterling, W. T. (2007). *Numerical Recipes with Source Code CD-ROM 3rd Edition: The Art of Scientific Computing*. Cambridge University Press.

Ricard, Y., Fleitout, L., & Froidevaux, C. (1984). Geoid heights and lithospheric stresses for a dynamic Earth. *Annales Geophysicae* (Vol. 2, No. 3, pp. 267-286).

Richards, M. A., & Hager, B. H. (1984). Geoid anomalies in a dynamic Earth. Journal of Geophysical Research: Solid Earth, 89(B7), 5987-6002.

Simon, J. L., Bretagnon, P., Chapront, J., Chapront-Touze, M., Francou, G., & Laskar, J. (1994). Numerical expressions for precession formulae and mean elements for the Moon and the planets. *Astronomy & Astrophysics*, 282(2), 663-683.

Schwiderski, Ernst W. (1985). On tidal friction and the decelerations of the earth's rotation and moon's revolution, *Marine Geodesy*, 9:4, 399-450.

Stacey, F. D., & Davis, P. M. (2008). *Physics of the Earth*. Cambridge University Press.

1304 Tian, Z., & Wisdom, J. (2020). Vertical angular momentum constraint on lunar formation and orbital history. 1305

Proceedings of the National Academy of Sciences, 117(27), 15460-15464.

1306 Williams, J. G., & Boggs, D. H. (2016). Secular tidal changes in lunar orbit and Earth rotation. *Celestial Mechanics*

1307 *and Dynamical Astronomy*, 126, 89-129.